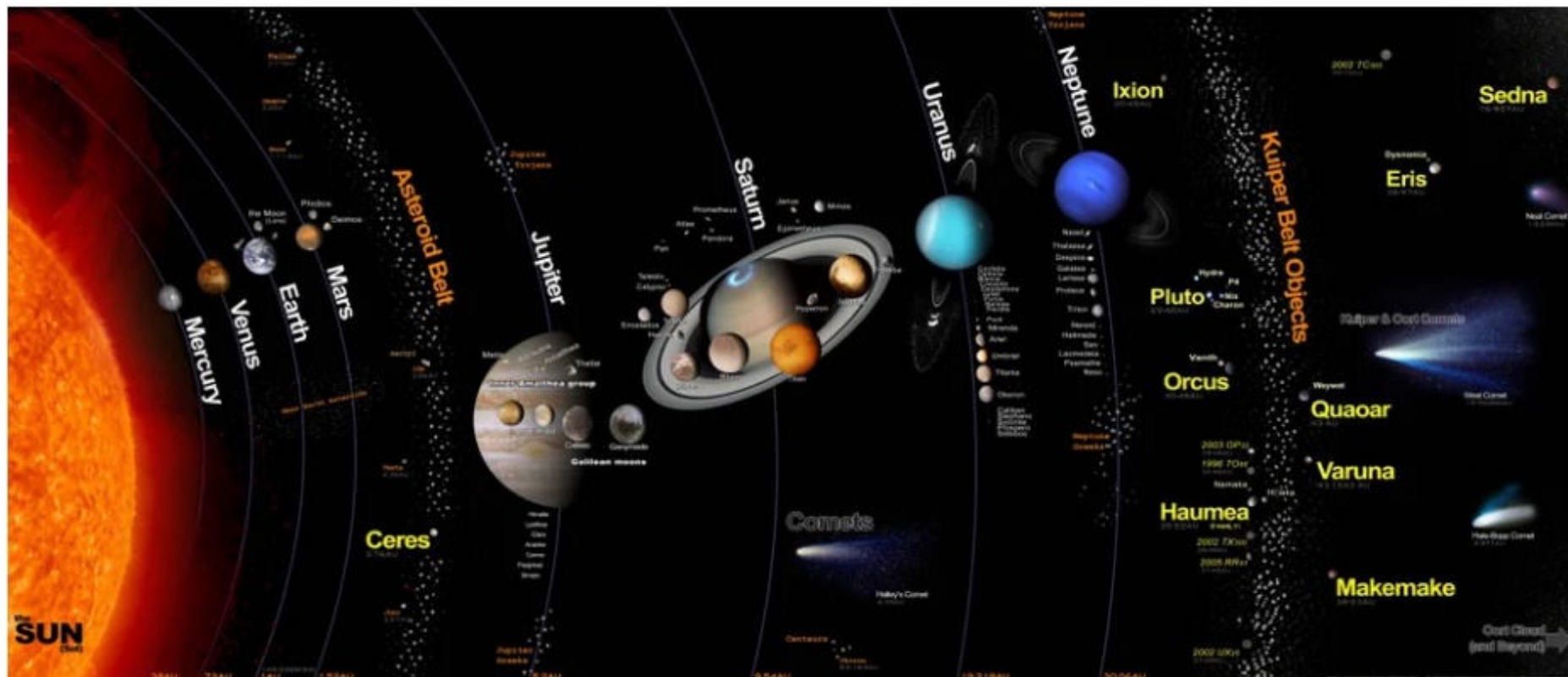


Planetology



Hélène Massol - GEOPS - U. Paris Saclay

Outline

1 – Solar system formation

2 - History of methods and studies of Earth Interior

3 - Internal structures of the Earth and mechanisms at play

4 – Other planets and exoplanets

5 – Habitable zone

Solar nebula theory

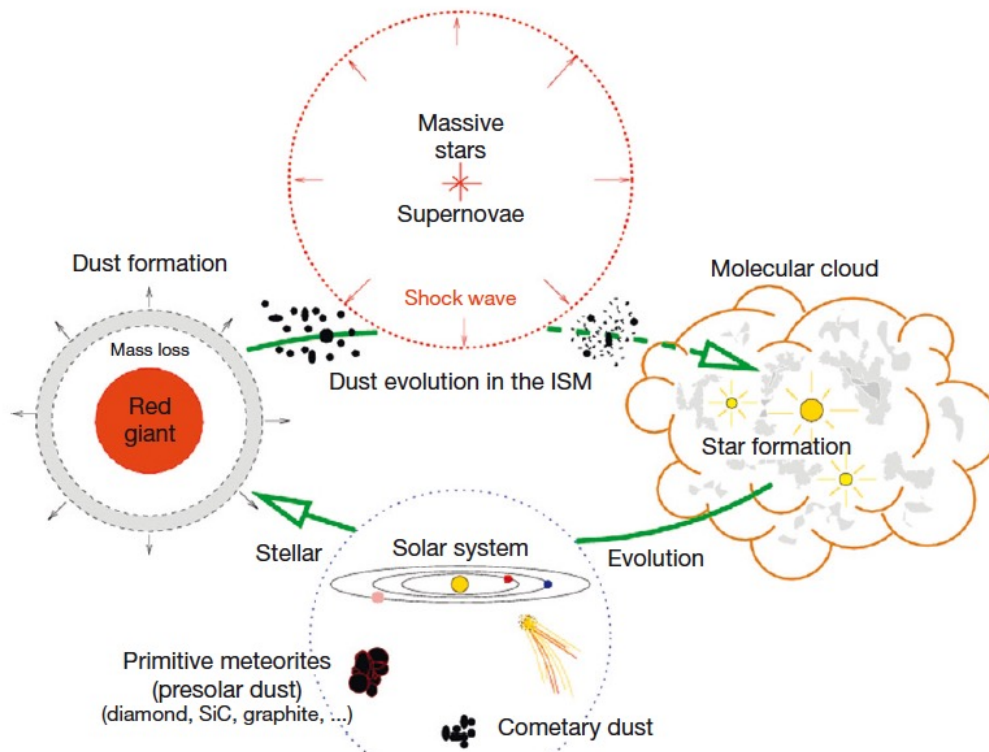


Figure 8 A schematic view of the life cycle of interstellar dust from its formation principally around evolved stars, and also to some extent in supernovae, to its incorporation into star-forming molecular clouds and planetary systems. Along the way, its properties evolve through energetic collisions with the gas and other grains in interstellar shock waves and through the effects of UV irradiation. Figure taken from Jones AP (2004) Dust destruction processes. In: Witt AN, Clayton GC, and Draine BT (eds.) *Astrophysics of Dust. ASP Conference Series*, Vol. 309, pp. 347–367. With permission from the Astronomical Society of the Pacific.

Palme et al. 2014

Solar nebula theory



Solar nebula theory



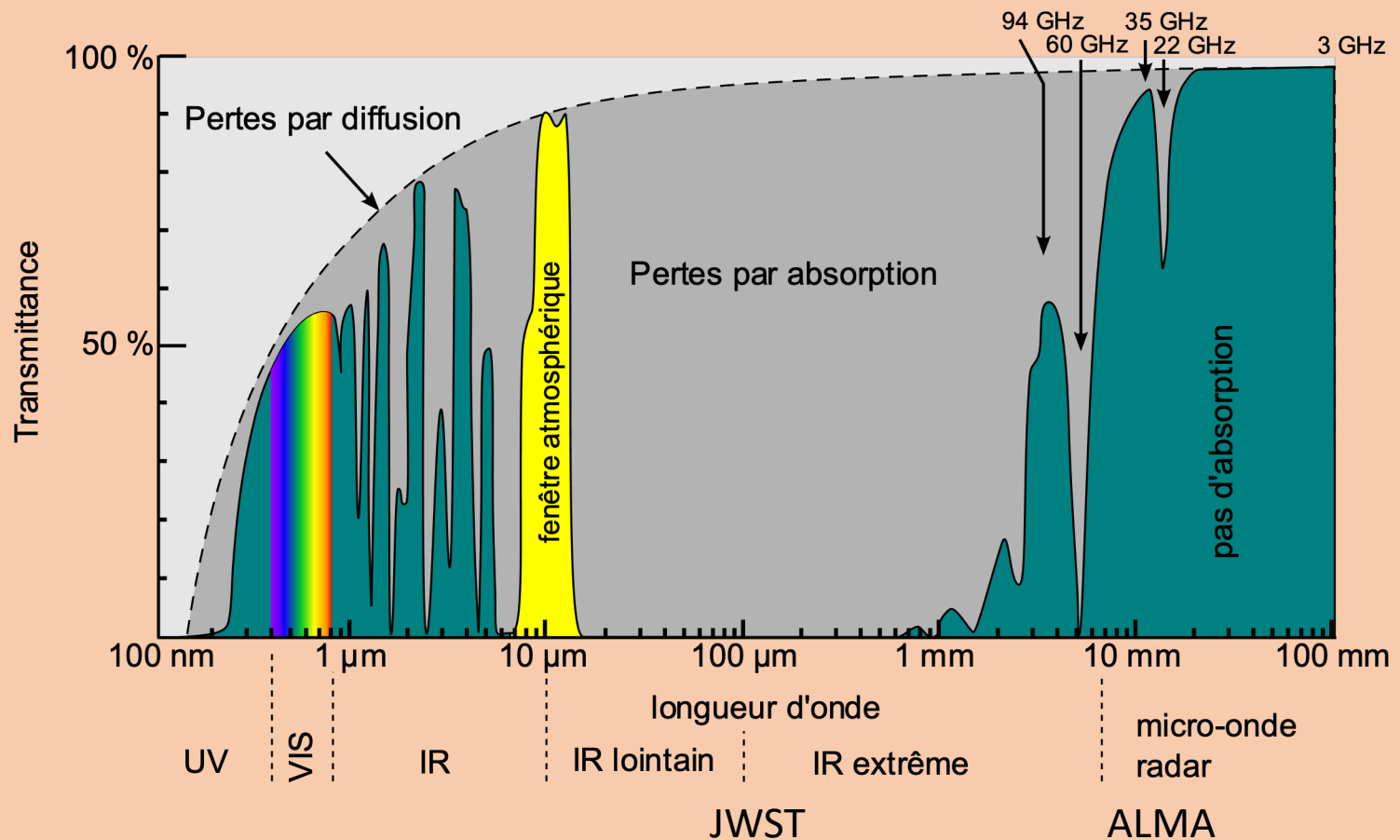
The inner region of the Orion Nebula as seen by both the Hubble Space Telescope (left) and the James Webb Space Telescope (right). Webb's sensitive infrared vision can peer through thick dust layers and see fainter stars, allowing scientists to study what is happening deep inside the nebula.

Show less ^

NASA/STSCI/RICE UNIV./C.O'DELL/ESA/CSA/PDRS4ALL ERS TEAM;
IMAGE PROCESSING OLIVIER BERNÉ

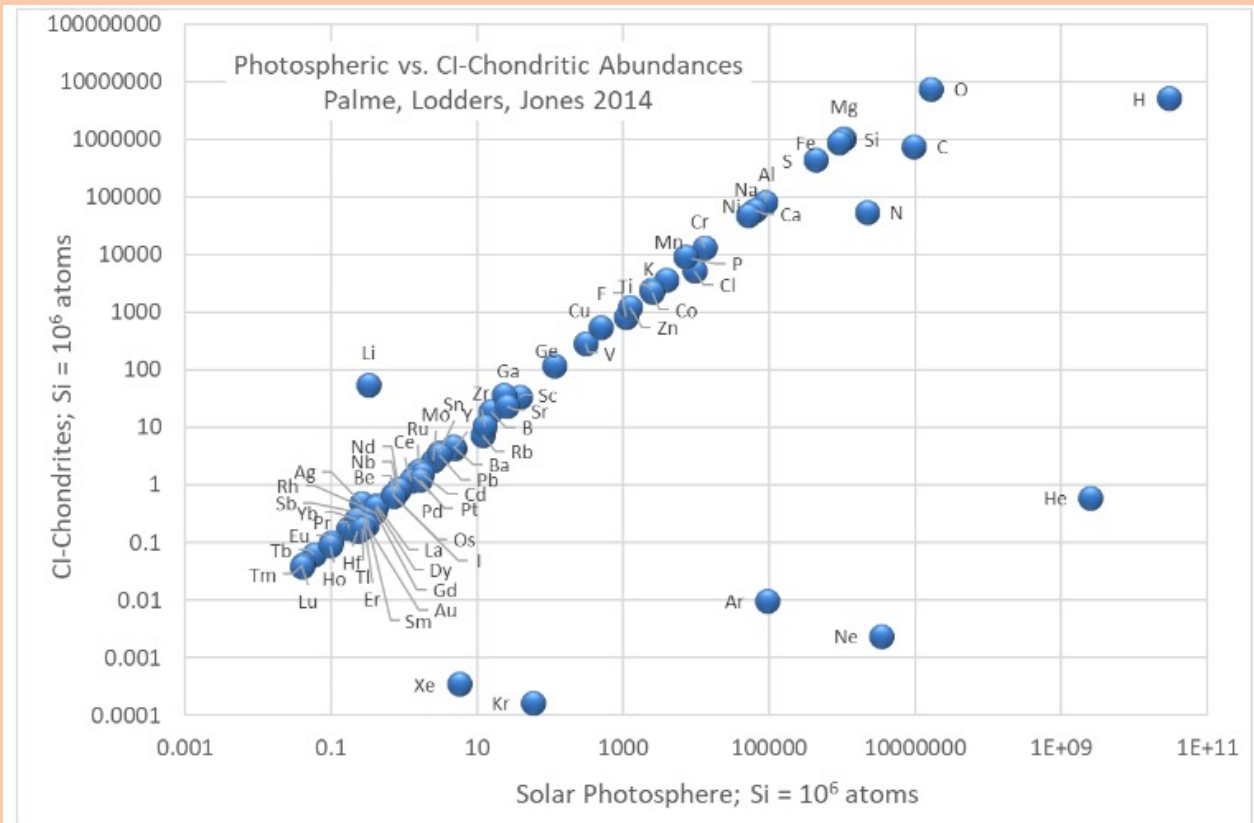
Solar nebula theory

Wavelengths



Solar nebula composition

Specie X	X/H
C	$2,91 \times 10^{-4}$
N	$8,02 \times 10^{-5}$
O	$5,81 \times 10^{-4}$
S	$1,83 \times 10^{-5}$
Si	$4,11 \times 10^{-5}$
Fe	$3,45 \times 10^{-5}$



from Planétologie, Sotin et al., Dunod

Figure 1. Atomic abundances of the elements in CI-chondrites versus abundances in the Sun (mainly photosphere). Both abundance sets are normalized to 10^6 silicon atoms. Perfect agreement would be along a 1:1 line and most elements plot along such a line within 10-20%. Despite some small scatter around the perfect correlation line, the correspondence over 13-orders of magnitude is impressive. Notable exceptions are Lithium, which is normal in meteorites but lost from the photosphere by diffusion into the sun and destroyed there; the other exceptions are elements (the noble gases, H, C, N, and O) that form highly volatile gases not retained in meteorites. Data from Palme et al. (2014).

Lodders , 2020

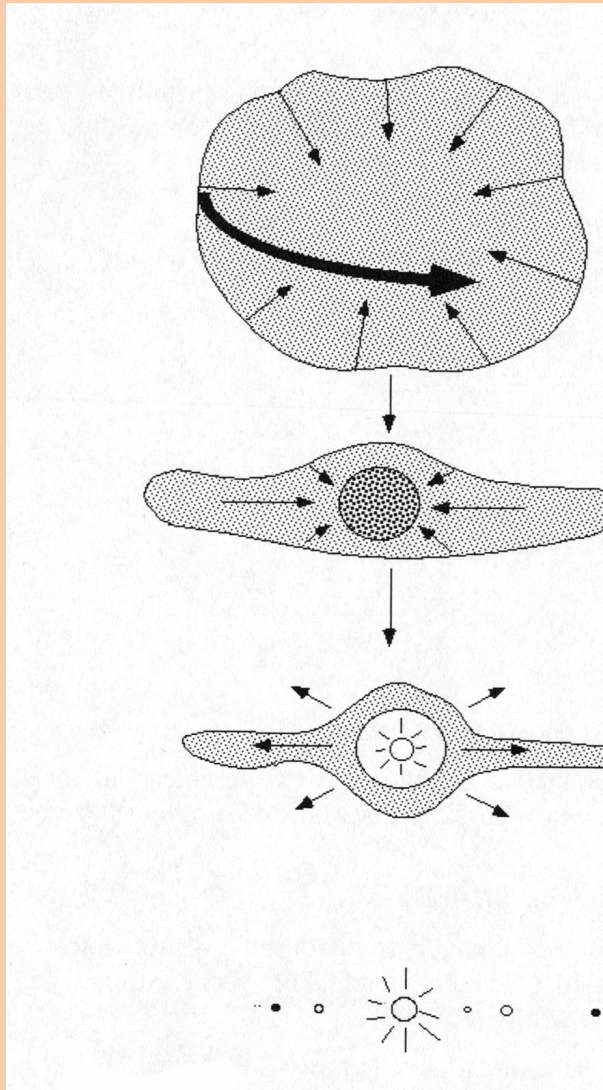
Solar system formation scenario

1- Collapse of the dense cloud (0.1-0.5 Ma)

2 - Structuration of an equatorial disk (0.05 Ma)

3-Accumulation of the sun (T. Tauri)
planetary accretion begins (1 -2 Ma).

4 – Dissipation of the disk gas by the solar wind (3 – 30 Ma)



from Planétologie, Sotin et al., Dunod

Solar nebula theory

(Initiated by E. Kant et P.S. Laplace au 18th century)

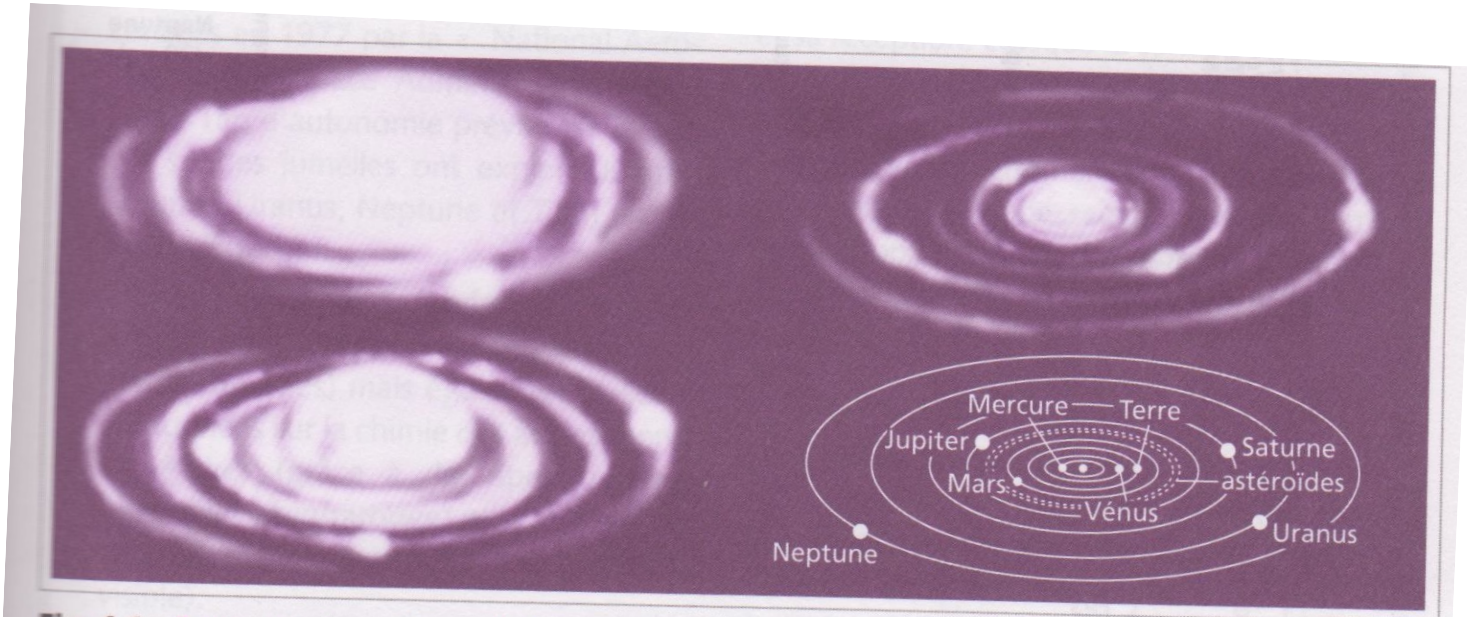
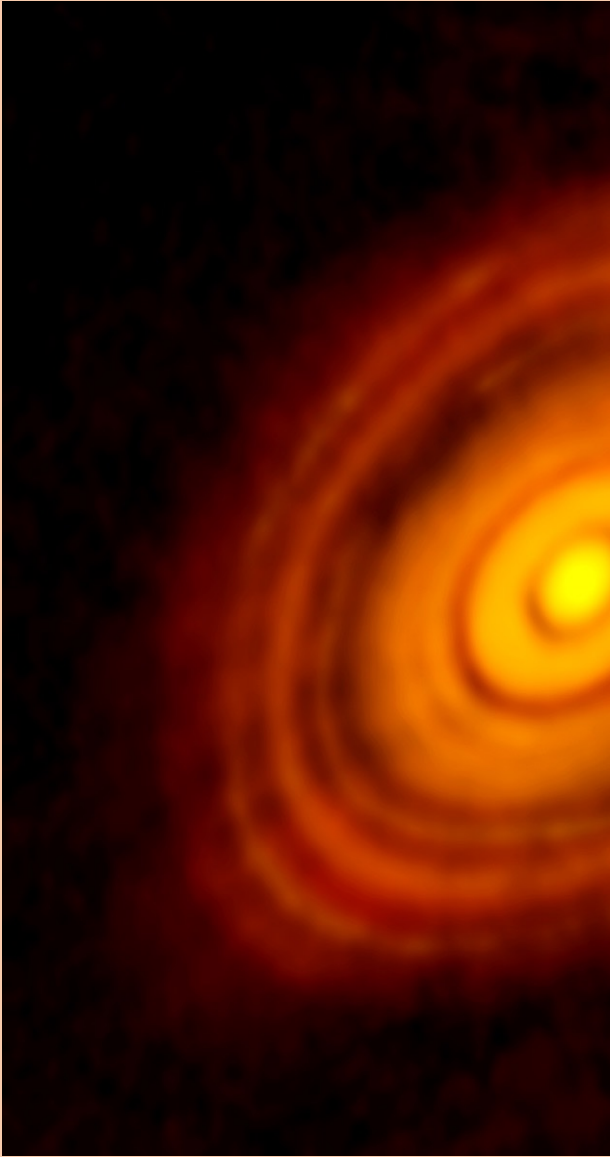


Fig. 4.1. Formation du système solaire : théorie de la nébuleuse solaire. D'après Prentice, 1978.

From Dewaele et Sanloup, éds Belin: l'Intérieur de la Terre et des planètes

Solar nebula theory

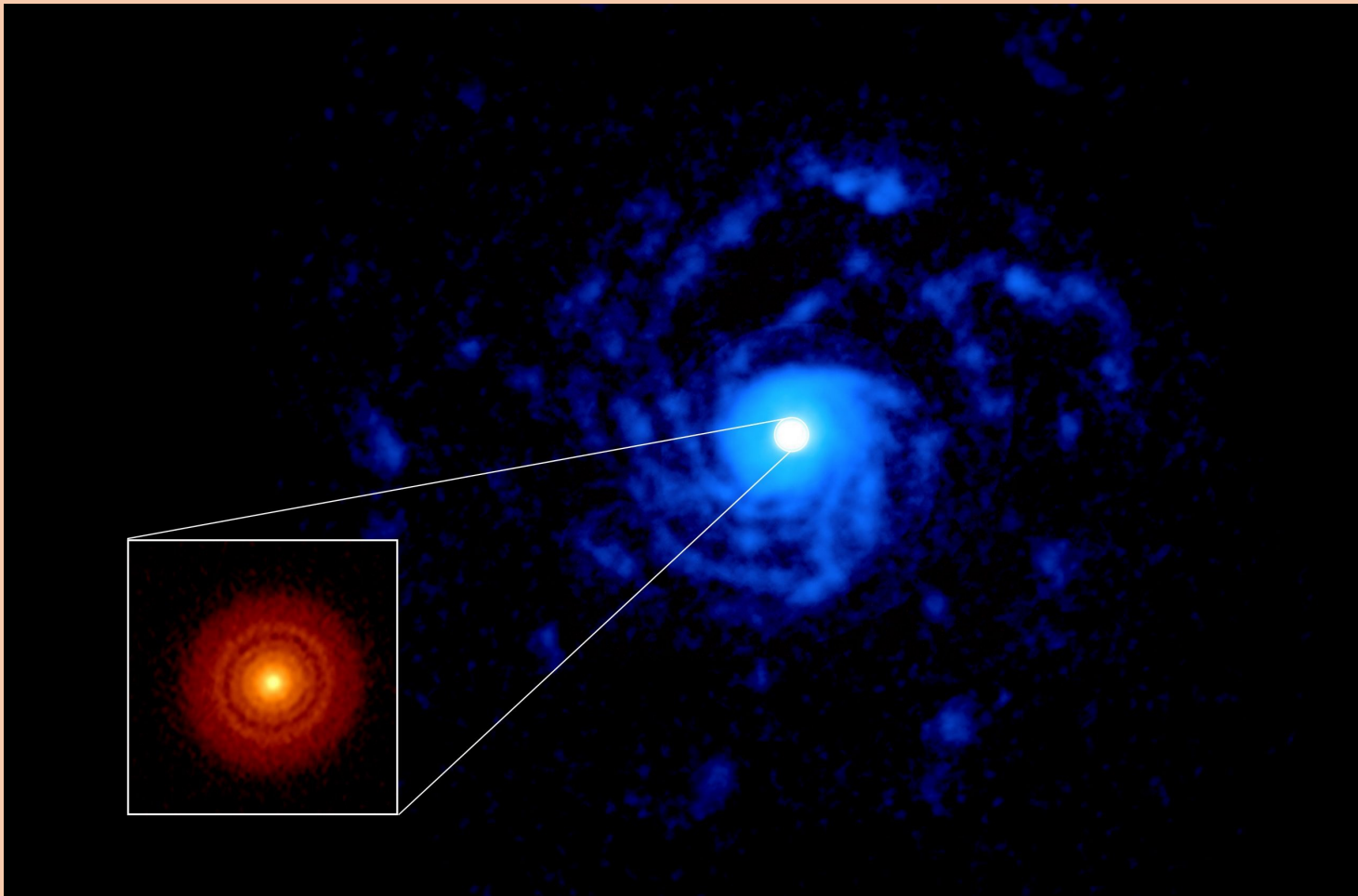


HL Tauri
Observed by ALMA
(Atacama Large
millimiter/submillimiter
Array):

Radiotelescope using
radar interferometry

<https://fr.wikipedia.org/wiki/Interférométrie>

Solar nebula theory



ALMA image of the planet-forming disk around the young star RU Lup. The inset image (lower left, red disk) shows a previous (DSHARP) observation of the dust disk with rings and gaps that hint at the presence of forming planets. The new observation shows a large spiral structure (in blue), made out of gas, that spans far beyond the compact dust disk.

Credit: ALMA (ESO/NAOJ/NRAO), J. Huang and S. Andrews; NRAO/AUI/NSF, S. Dagnello

Introduction / constraints: chronology of events

Dissipation of gas in the protoplanetary gas confirmed around
10 My by datation using short lived Pd-Ag system on Iron meteorites (Hunt et al., 2022)

Constraints on the time of formation of Earth

Hf-W + U Pb: ~30 – 100 My and Mars : 1 – 10 My measured on martian meteorites

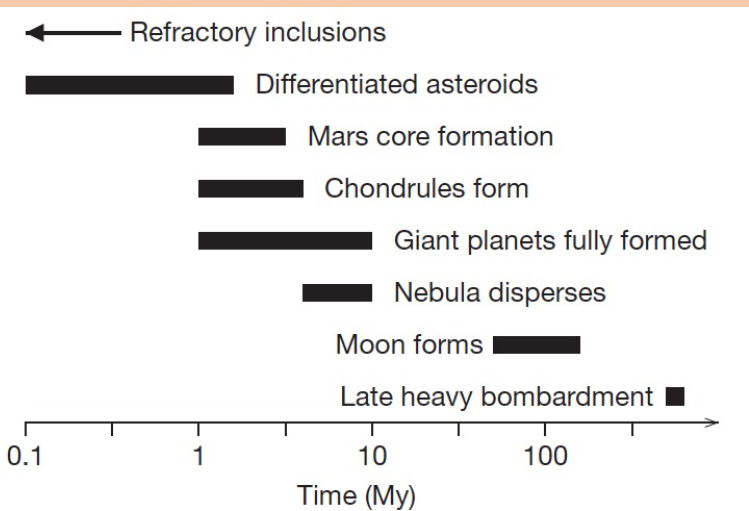
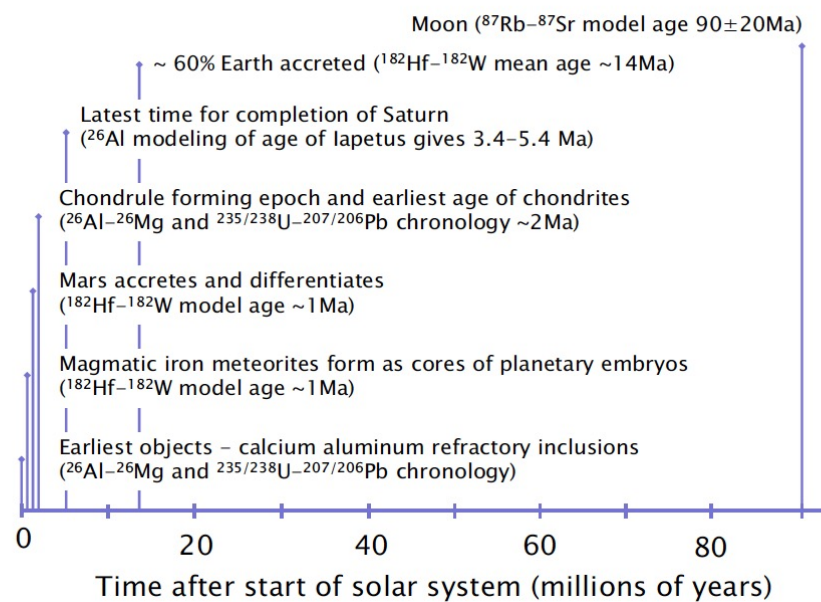


Figure 1 The timing of events in the early Solar System (Data and models: Dauphas and Pourmand, 2011; Hutcheon et al., 2009; Movshovitz et al., 2010; Qin et al., 2008; Sung et al., 2009; Touboul et al., 2007).

Chambers, 2014



Encyclopedia of the solar system

Condensation and accretion

Boss, 1998

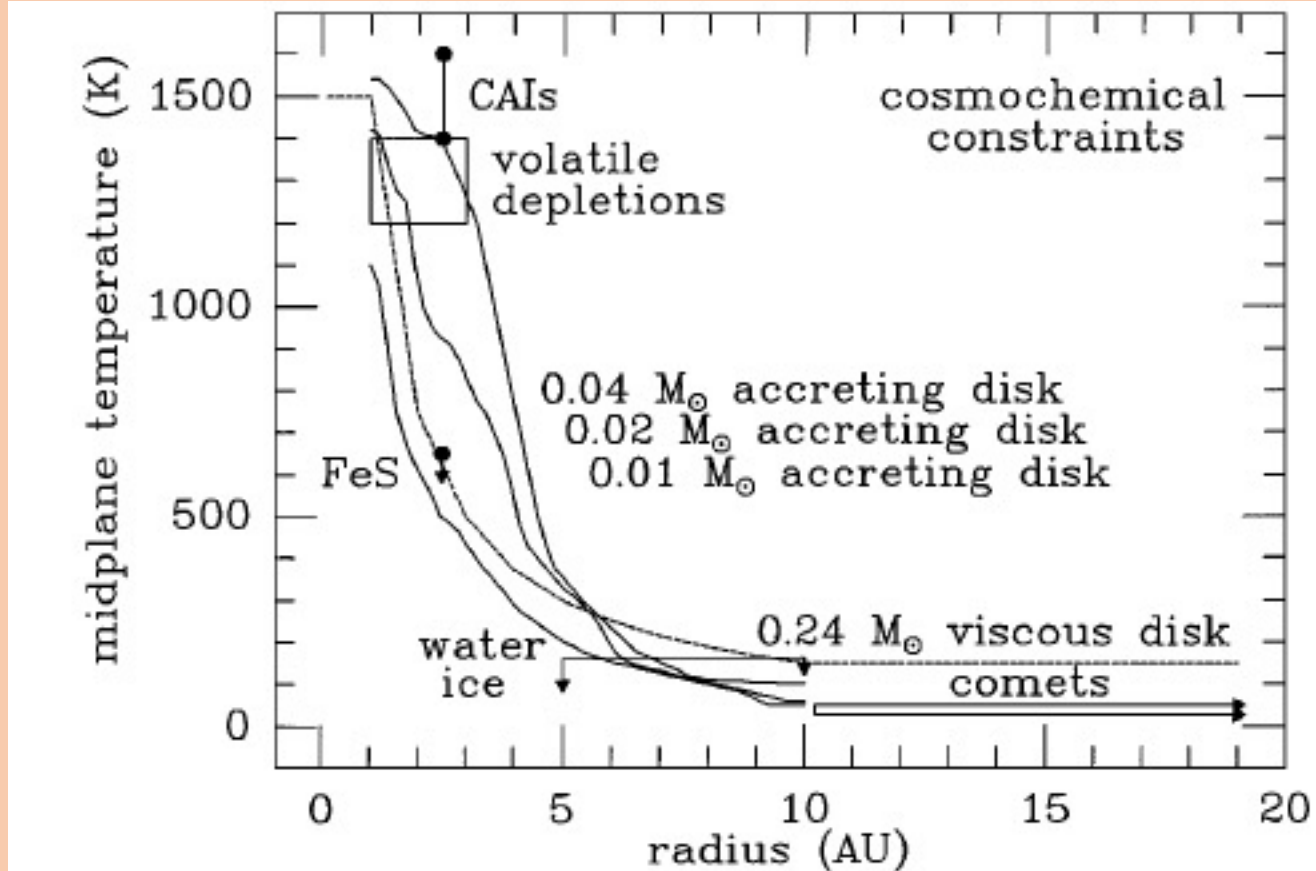
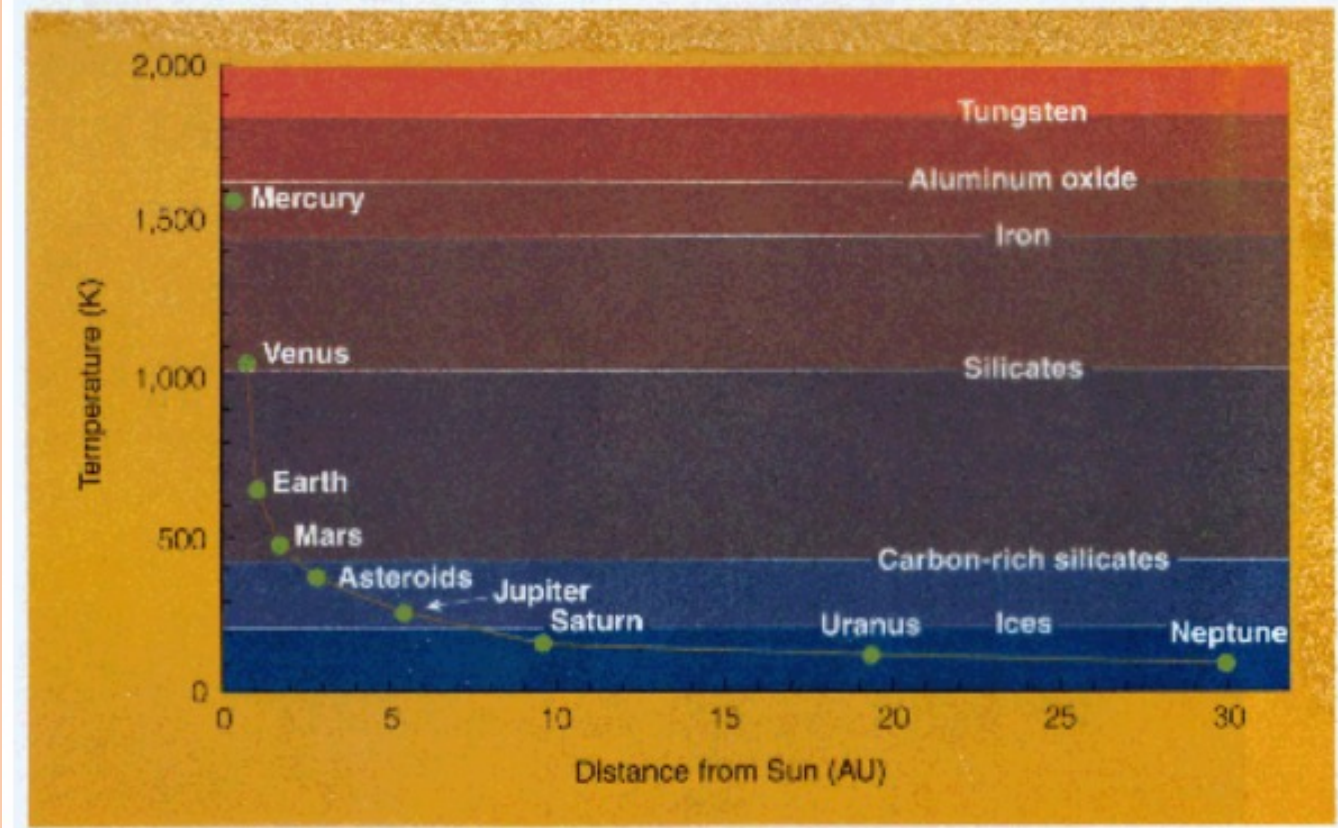


Figure 1 Comparison with theoretical models of cosmochemically derived constraints on disk midplane temperatures (CAIs, volatile depletions, FeS, water ice, and comets; see text for references). Solid lines are values of T_m for three Ansatz disk models (Boss 1996a), labeled from top to bottom by the disk masses (inside 10 AU). Dashed line is T_m for a viscous accretion disk model (Morfill 1988) with $\alpha = 10^{-2}$, $\dot{M} = 10^{-5} M_{\odot}/\text{year}$, and a mass of $0.24 M_{\odot}$ inside 10 AU.

Condensation and accretion

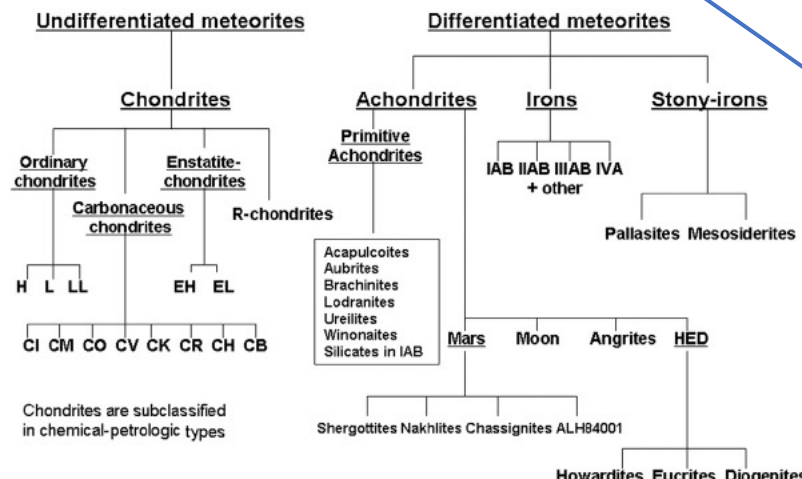
- Refractory elements $T_c > 1400$ K
- Volatiles $T_c < 800$ K

Condensation of different chemicals



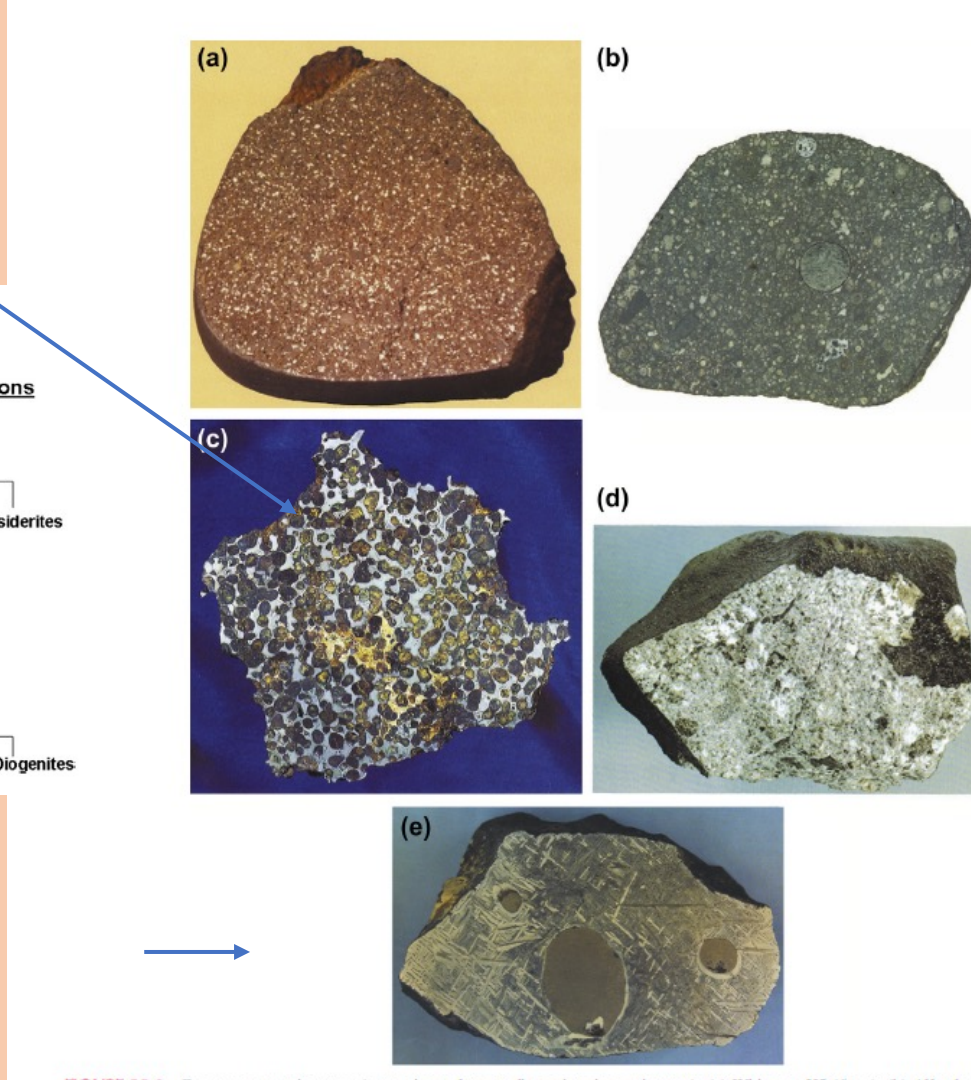
Condensation and accretion: meteorites

from mantle core
interface



Core fragments

Lipschutz, 2015



Solidified
magma

FIGURE 28.6 Common meteorite types (approximate longest dimension, in centimeters): (a) Whitman, H5 (6 cm); (b) Allende; C3V (8 cm)—note 1 cm chondrule in center, (c) Springwater pallasite (18 cm); (d) Sioux Co. eucrite (8 cm); (e) Sanderson IIIB medium octahedrite (13 cm)—note large FeS inclusions.

Momentum conservation (or Newton's second law)

When in a continuum medium subjected to external forces

$$\tau_z = \frac{dL_z}{dt}$$

<https://www.youtube.com/watch?v=ko52m9jGTQ>

$$L_z = I\omega_z$$

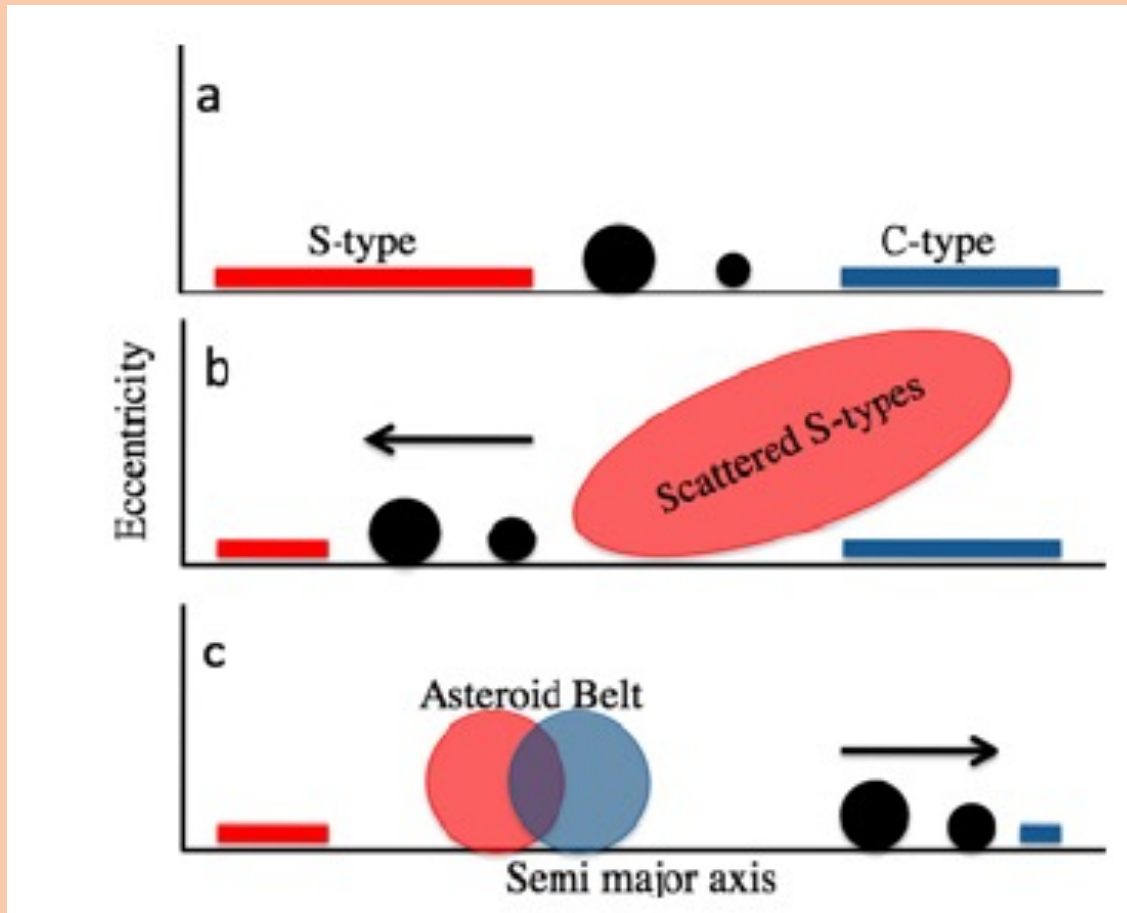
Where τ_z represent the sum of the
Moments of the external forces exerted on M

With $I_\Delta = \sum_i m_i r_i^2$

In a continuum: $I_\Delta = \iiint_V d^2 \rho dV$

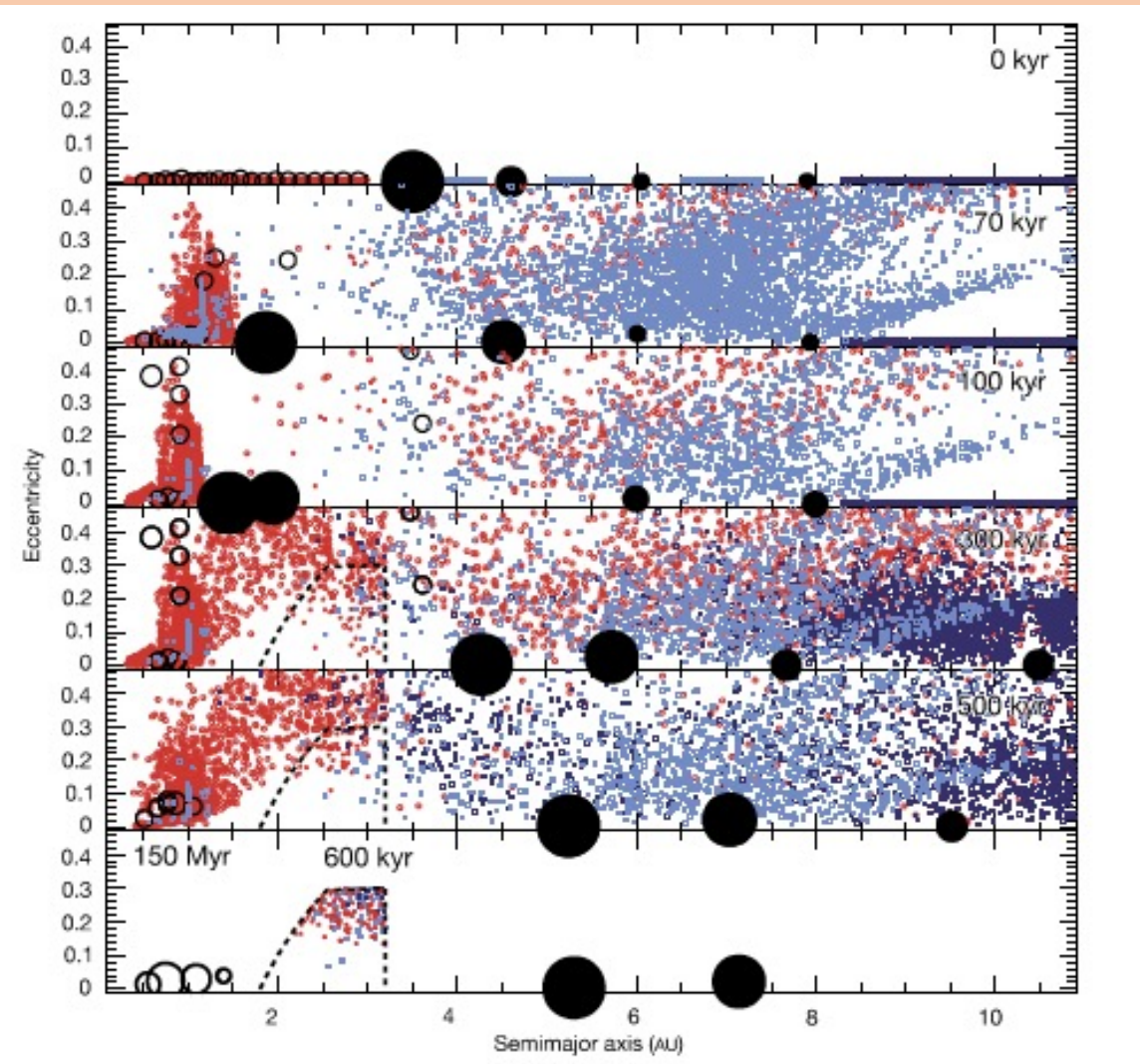
e.g. In the case of an homogeneous sphere $I_\Delta = 0.4Mr^2$

Condensation and accretion



Walsh et al., 2012

Condensation and accretion



O'Brien, 2018

Fig. 3 Figure from Walsh et al. (2011) showing a simulation of the Grand Tack scenario. The *top three panels*

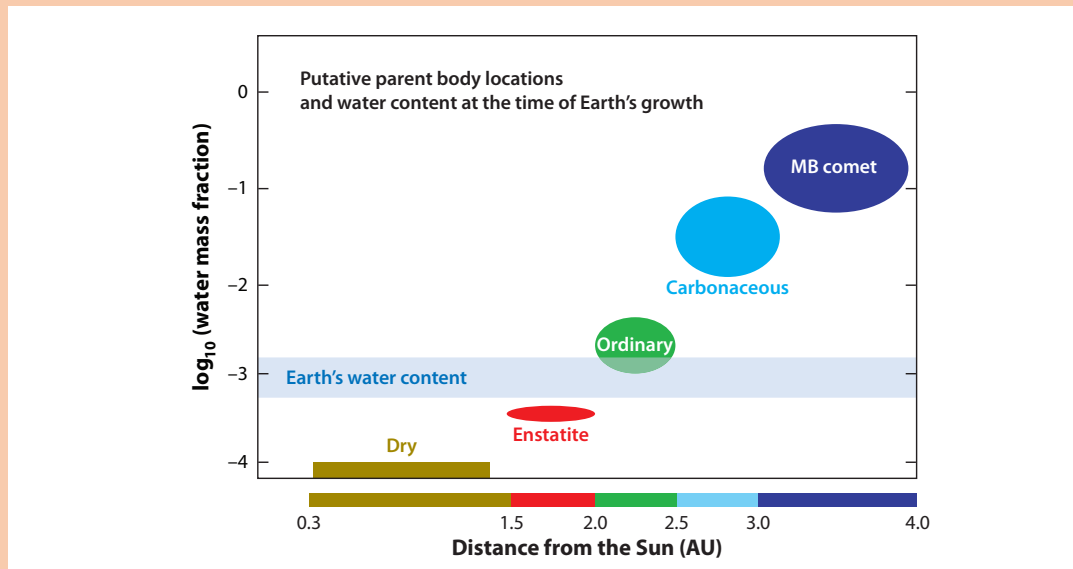
Summary

Within the disk, planetary migration can occur inward or outward depending on
The viscosity, gas pressure and mass of the forming planet
See Kley and Nelson 2012 for review

<https://www.youtube.com/watch?v=nwSNU3-m0ew>

Questions:

How much water was accreted?



Morbidelli, 2012

Are all stellar system underwent the same accretion processes and timing?
Contribution to come from exoplanetary systems studies

Earth radius measured by Erasthene (erroneous $\approx 15\%$; 205 BC)

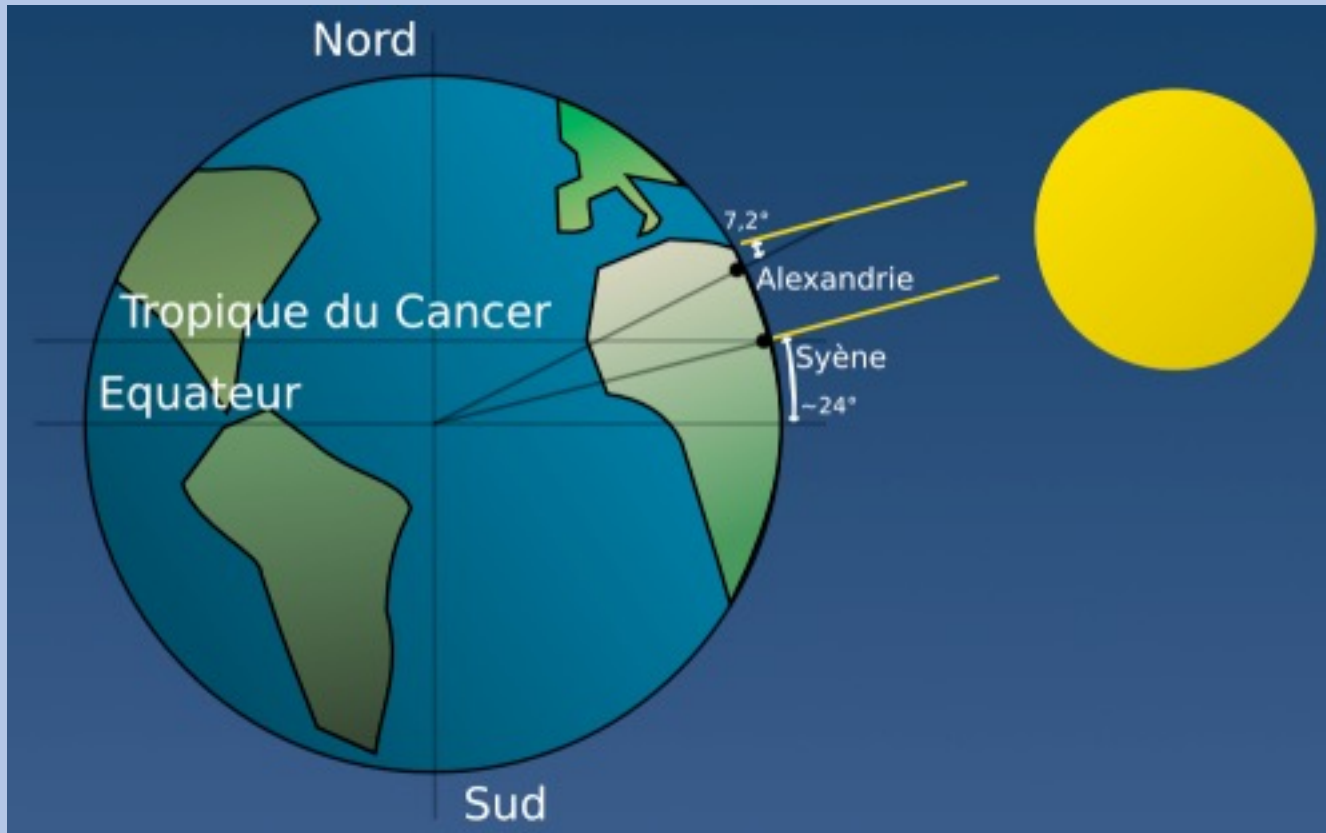
Modern geodesy: **6371 km**

Mass of Earth deduced from the gravitation law (Newton 1687).

Constant of gravitation needs to be measure **G**

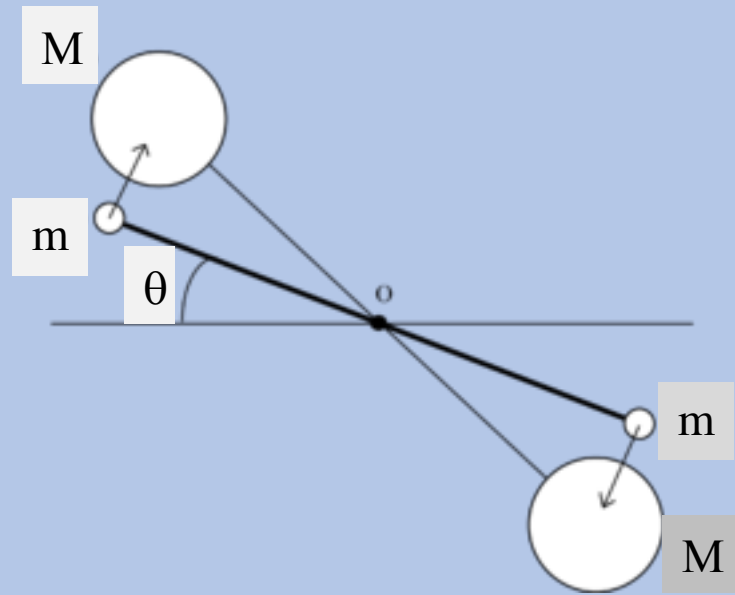
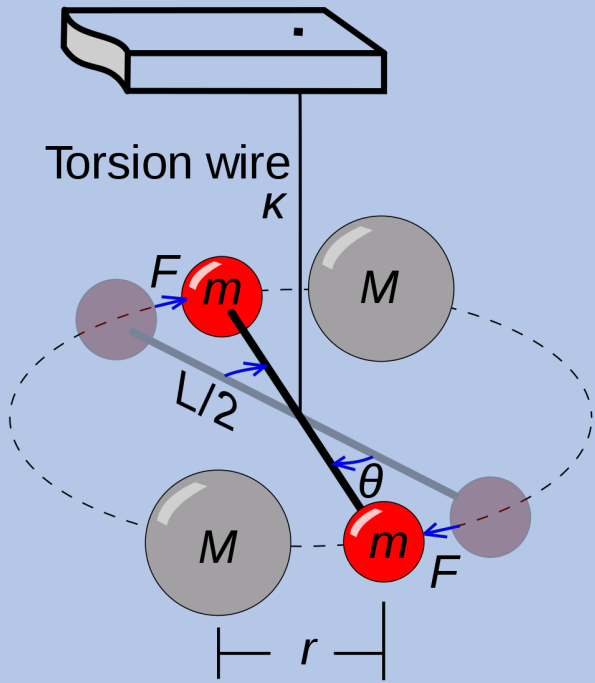
Radius of the Earth

Measuring the radius of the Earth: 6270 km
Distance Alexandria - Syene: 787,5 km



http://fr.wikipedia.org/wiki/Fichier:Eratosthene_mesure_terre.png

Cavendish torsion balance



Cavendish measure G in **1798** and this allows for

Earth mass: **$5.97 \cdot 10^{24} \text{ kg}$**

$$\rho = 5.52 \cdot 10^3 \text{ kg m}^{-3}.$$

Rock surface densities vary from

1.5 to $3.2 \cdot 10^3 \text{ kg m}^{-3}$ -> **dense rocks at the center.**

Mass + Moment of inertia => a first two layer model

Core radius estimated $\approx 3485 \text{ km}$ by **Gütenberg, 1912**

Two layers model

$$I_t = 0.331 MR^2$$

$$I_s = 0.4 MR^2$$

$$M_t = 5.97 \cdot 10^{24} \text{ kg}$$

$$R = 6371 \text{ km}$$

$$R_n = 3485 \text{ km}$$

Core radius inferred \approx
3485 km by Gutenberg, 1912

$$r_N = 12\,430 \text{ kg m}^{-3}$$

$$r_M = 4160 \text{ kg m}^{-3}$$

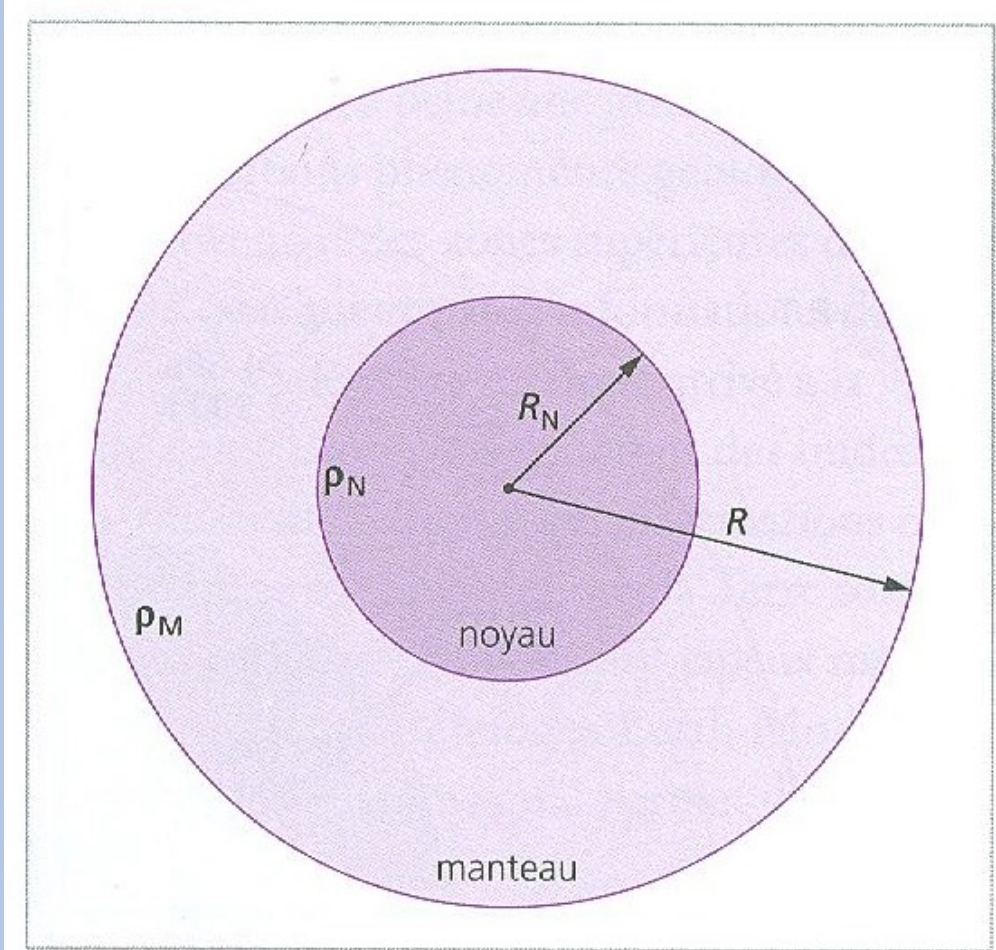


Fig. 2. Modèle de Terre à deux enveloppes. On distingue le manteau (M) et le noyau (N).

From Dewaele et Sanloup, éds Belin: l'Intérieur de la Terre et des planètes

Internal structure of the Earth

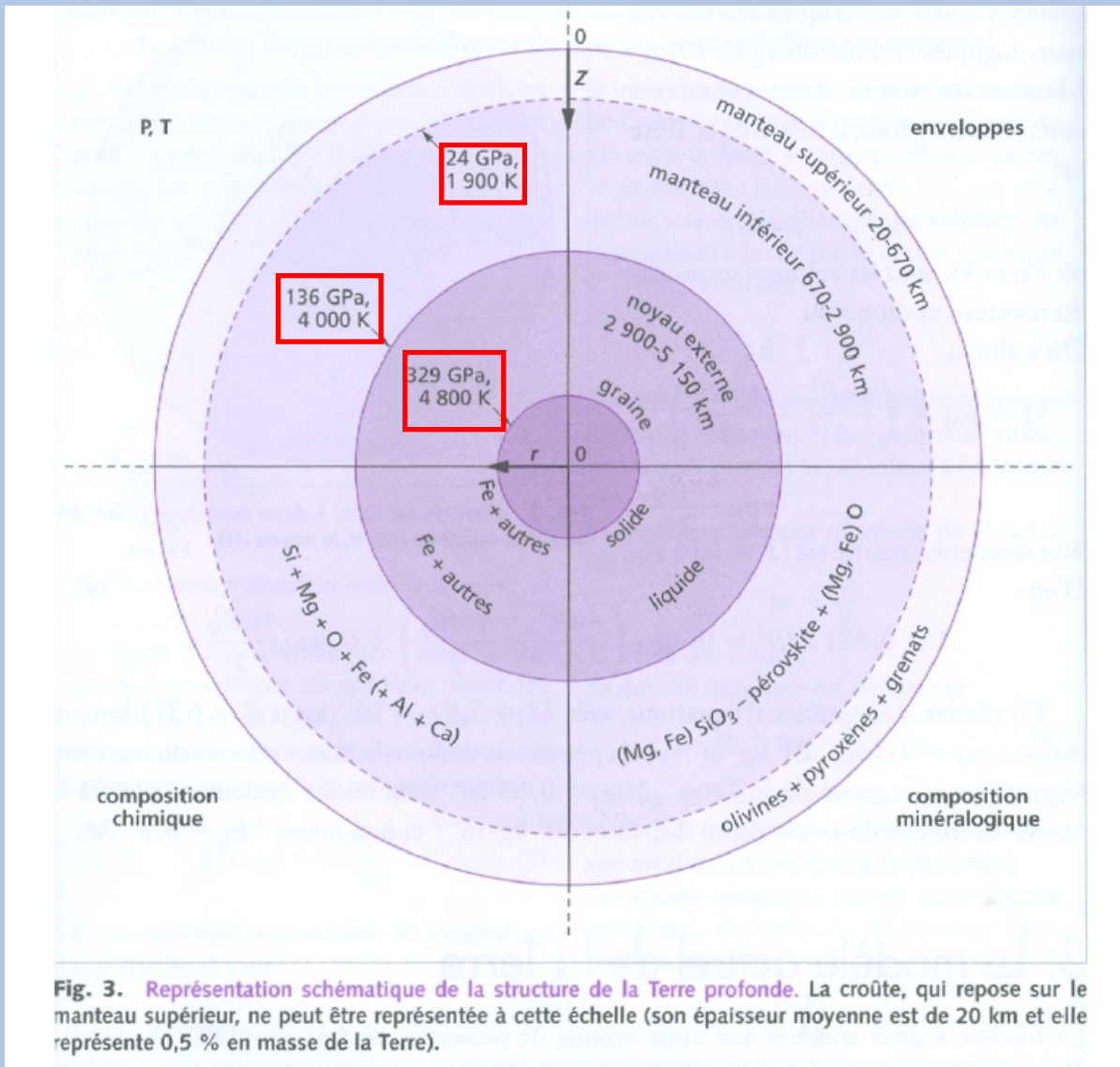
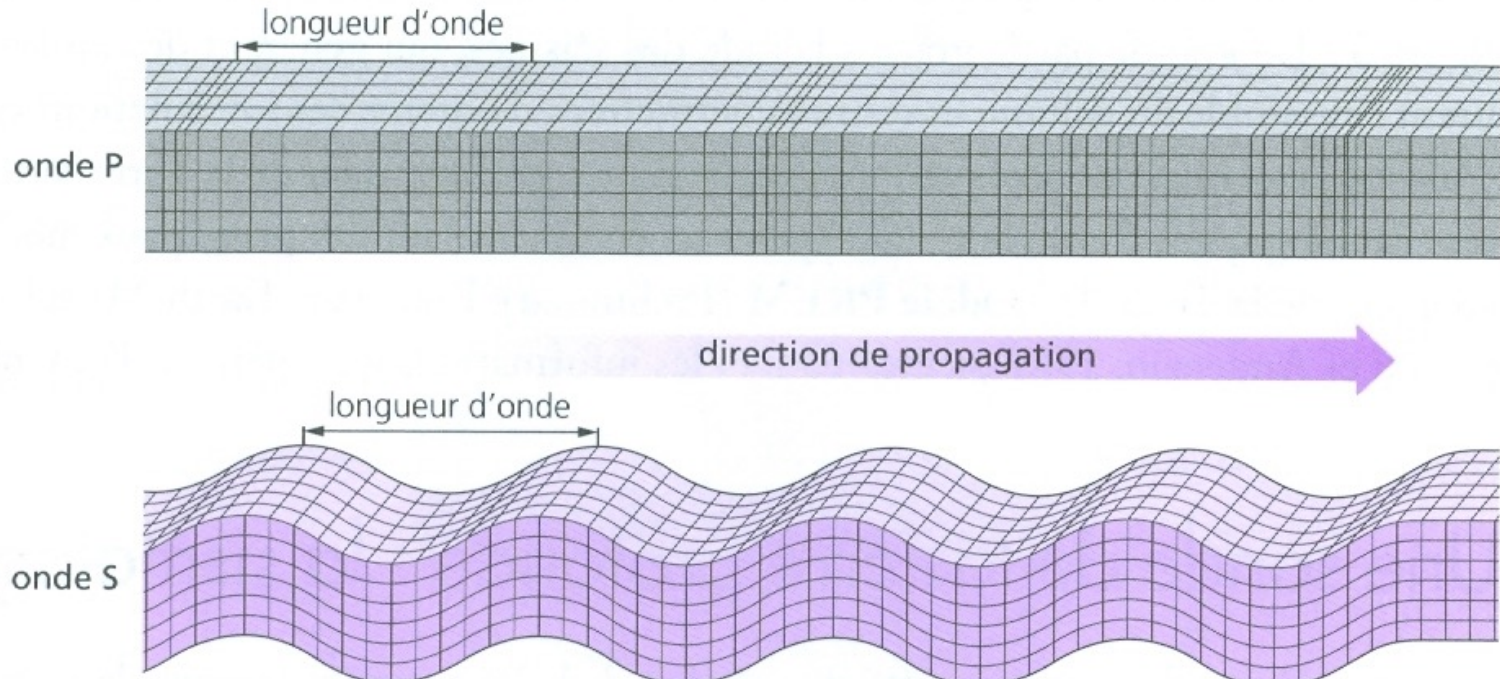


Fig. 3. Représentation schématique de la structure de la Terre profonde. La croûte, qui repose sur le manteau supérieur, ne peut être représentée à cette échelle (son épaisseur moyenne est de 20 km et elle représente 0,5 % en masse de la Terre).

From: Dewaele et Sanloup, éds Belin:
l'Intérieur de la Terre et des planètes



$$V_p = \sqrt{\frac{4\mu / 3 + K_s}{\rho}}$$

$$V_s = \sqrt{\frac{\mu}{\rho}}$$

Fig. 4. Déformations d'un milieu parcouru par une onde P ou une onde S.

K_s : module of incompressibility

μ : shear modulus

Sismology

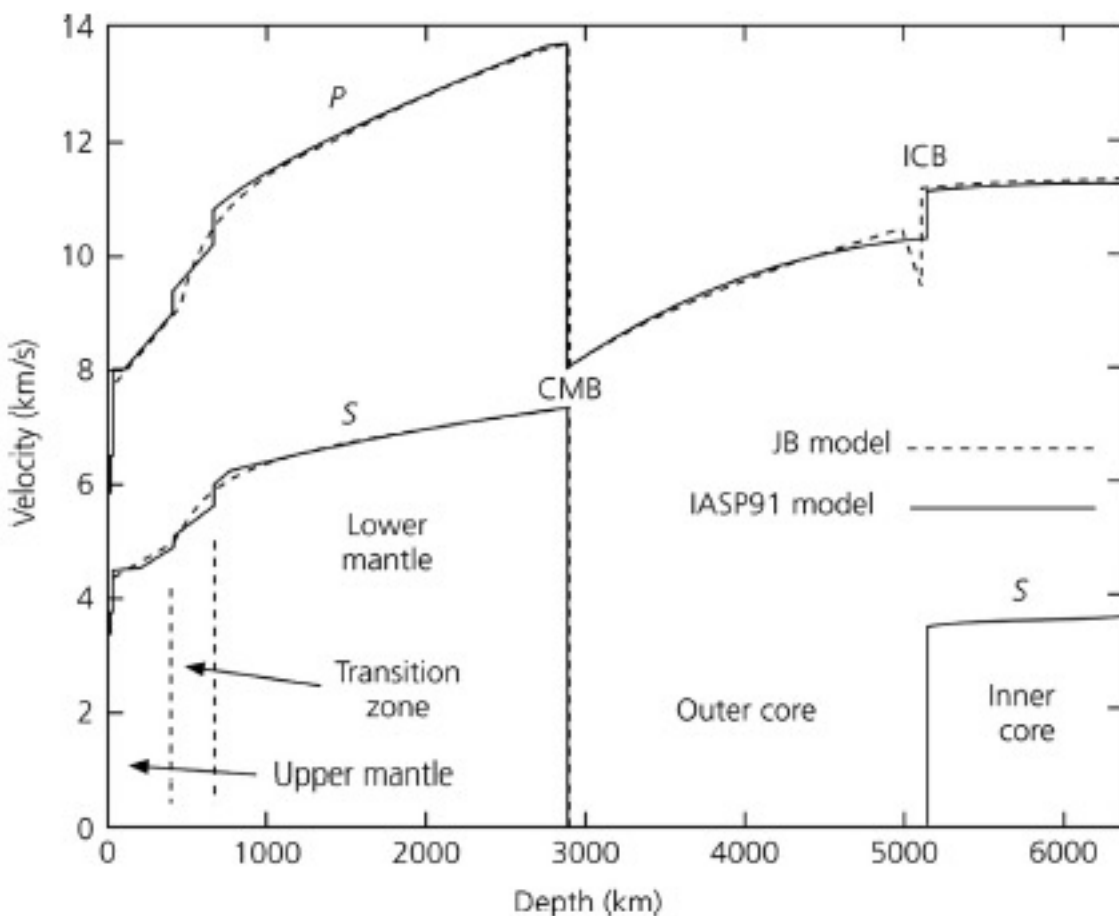


FIGURE 21.14 Model Comparisons. Comparison of a velocity model by Jeffreys (c. 1937) with model IASP91. Notice that for the most part changes have been minor, except for the discontinuities in the transition zone, solidity of the inner core, and structure just above inner core boundary.

From encyclopedia

Density profile

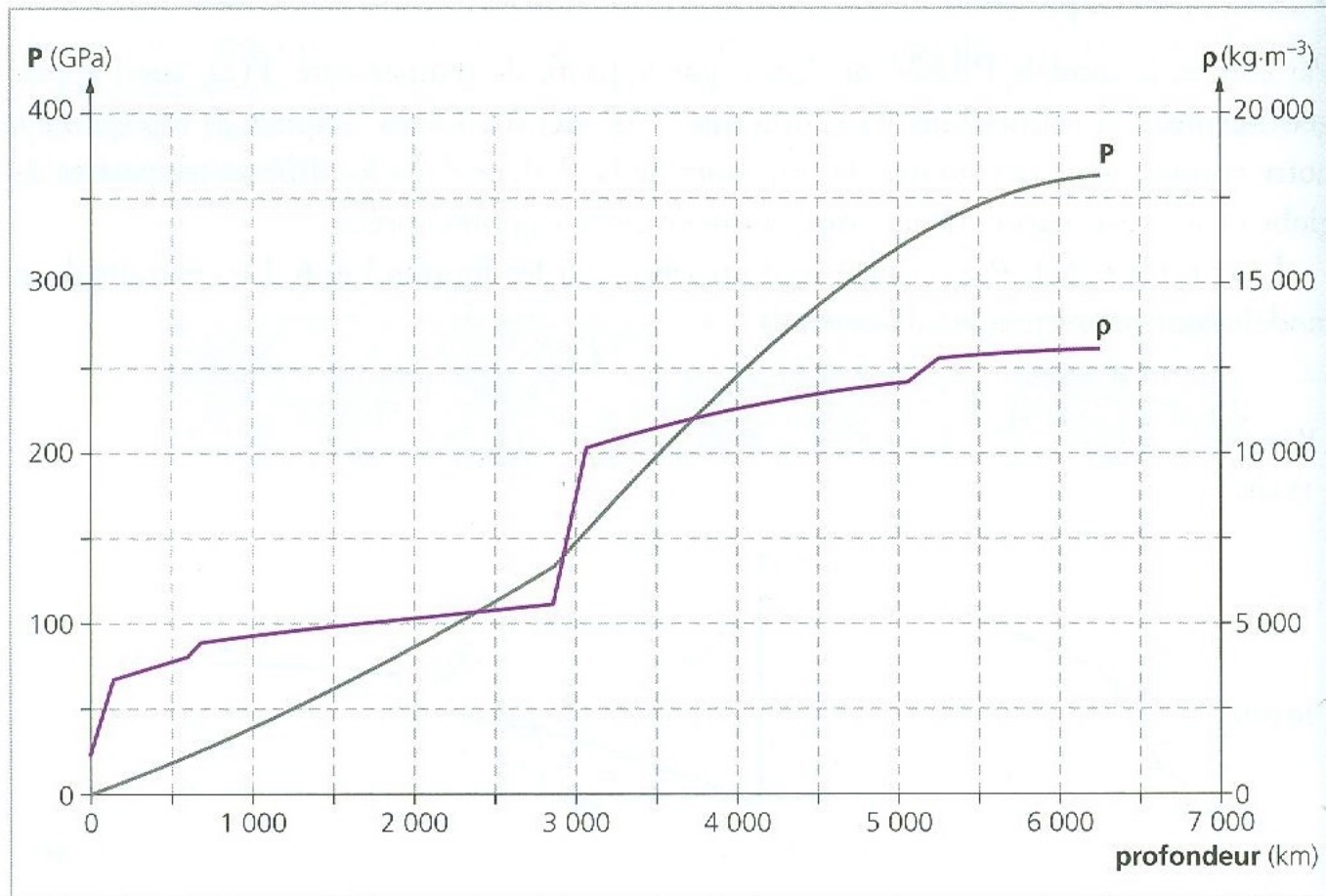


Fig. 6. Profils de masse volumique (ρ) et de pression (P). P et ρ sont représentés en fonction de la profondeur (modèle PREM).

from Dewaele et Sanloup, éds Belin: l'Intérieur de la Terre et des planètes

Francis Birch (1903-1992): mantle = ferromagnesium silicates

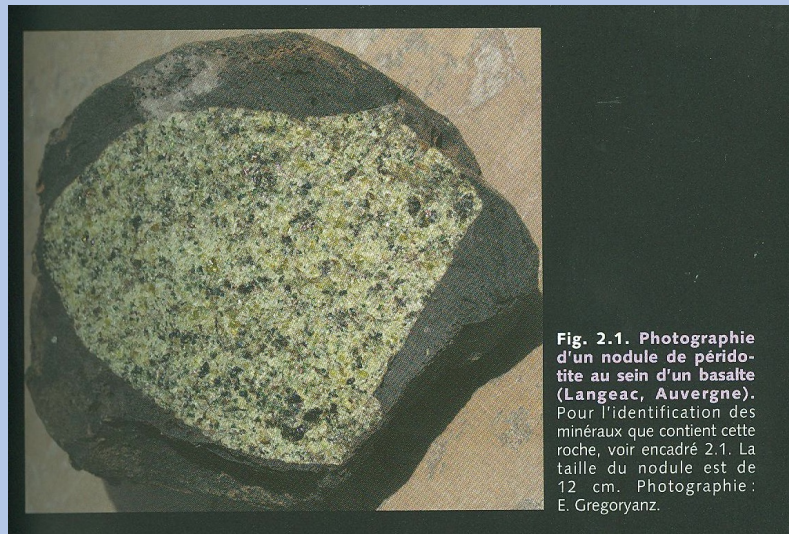


Fig. 2.1. Photographie d'un nodule de péridotite au sein d'un basalte (Langeac, Auvergne). Pour l'identification des minéraux que contient cette roche, voir encadré 2.1. La taille du nodule est de 12 cm. Photographie: E. Gregoryanz.

Phase change in between 300 et 900 km
Confirmed by Ringwood in 1956.

Core: solid iron inner core; liquid iron outer core

Phase changes in the mantle

Olivines $(\text{Mg}_{1-x}\text{Fe}_x)\text{SiO}_4$:
 Mg_2SiO_4 :forsterite, Fe_2SiO_4 : Fayalite

Orthopyroxènes $(\text{Mg}_{1-x}\text{Fe}_x)\text{SiO}_3$ MgSiO_3 :
Enstatite ; FeSiO_3 : ferrosilite

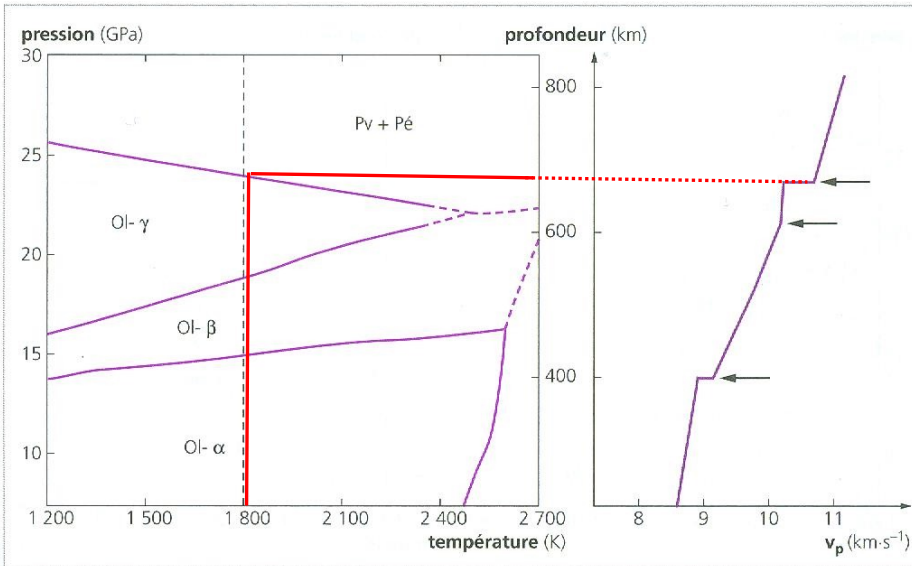


Fig. 2.3. Diagramme de phase de la forstérite Mg_2SiO_4 . Le profil de vitesse sismique v_p du modèle PREM, en fonction de la profondeur correspondant à la pression, est donné pour comparaison. La ligne verticale indique la température de 1800 K, température approximative du manteau à ces profondeurs. Ol- α : Mg_2SiO_4 phase α , Ol- β : Mg_2SiO_4 phase β (structure spinelle modifiée), Ol- γ : Mg_2SiO_4 phase γ (structure spinelle), Pv : MgSiO_3 -pérovskite, Pé : périclase MgO . Flèches : principales discontinuités des vitesses sismiques. Inspiré de S.-H. Shim et coll., 2001, et J.-P. Poirier, 1991b.

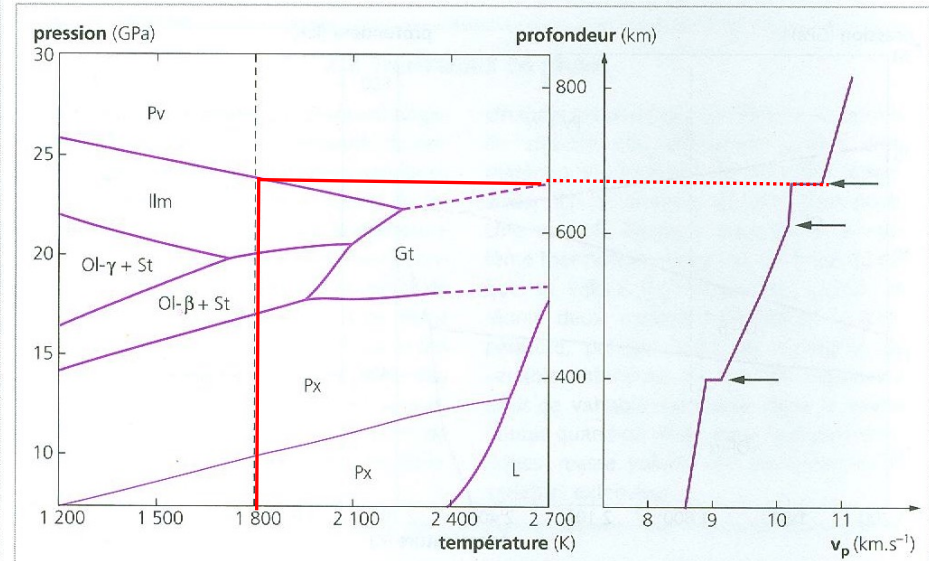


Fig. 2.4. Diagramme de phase de l'enstatite MgSiO_3 . Le profil de la vitesse sismique v_p du modèle PREM, en fonction de la profondeur correspondant à la pression, est donné pour comparaison. La ligne verticale indique la température de 1800 K, température approximative du manteau à ces profondeurs. Px : pyroxène, Ol- β : Mg_2SiO_4 phase β (structure spinelle modifiée), Ol- γ : Mg_2SiO_4 phase γ (structure spinelle), Gt : MgSiO_3 structure grenat, IIm : MgSiO_3 -ilmenite, St : stishovite SiO_2 , Pv : MgSiO_3 -pérovskite. La ligne fine indique la transition orthopyroxène \rightarrow clinopyroxène. Flèches : principales discontinuités des vitesses sismiques. Inspiré de Chopelas, 1999 et Gasparik, 2003.

From Dewaele et Sanloup, éds Belin: l'Intérieur de la Terre et des planètes

Principal phase name is perovskite synthetised in the laboratory (can be found in some meteorites)

Active mantle

Evidences: lithosphere deformation, volcanism,
plate tectonics

cooling of the Earth

Topography, plates

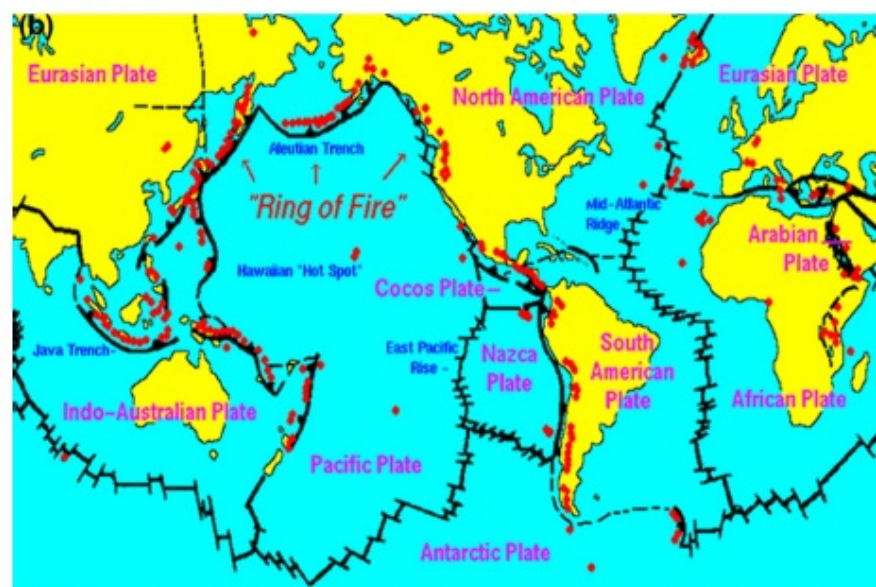
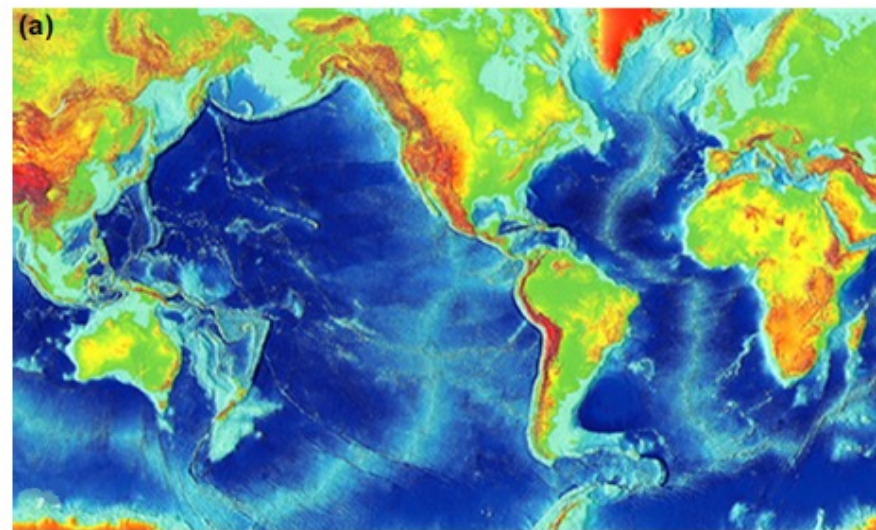
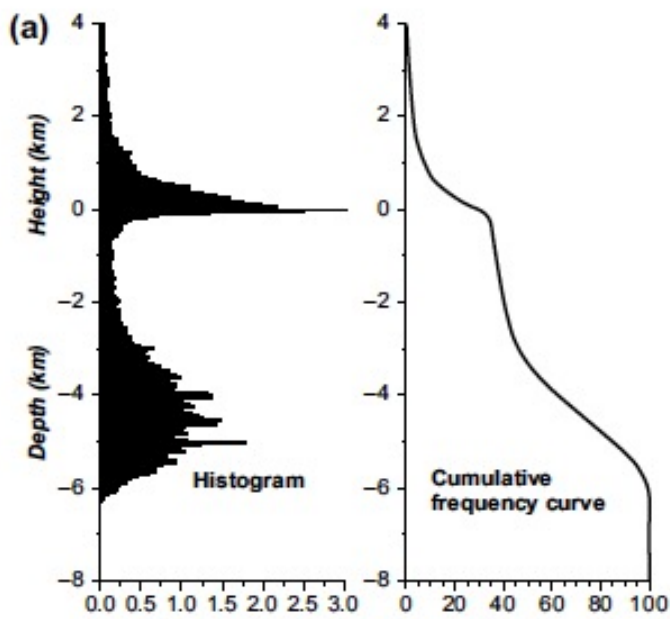
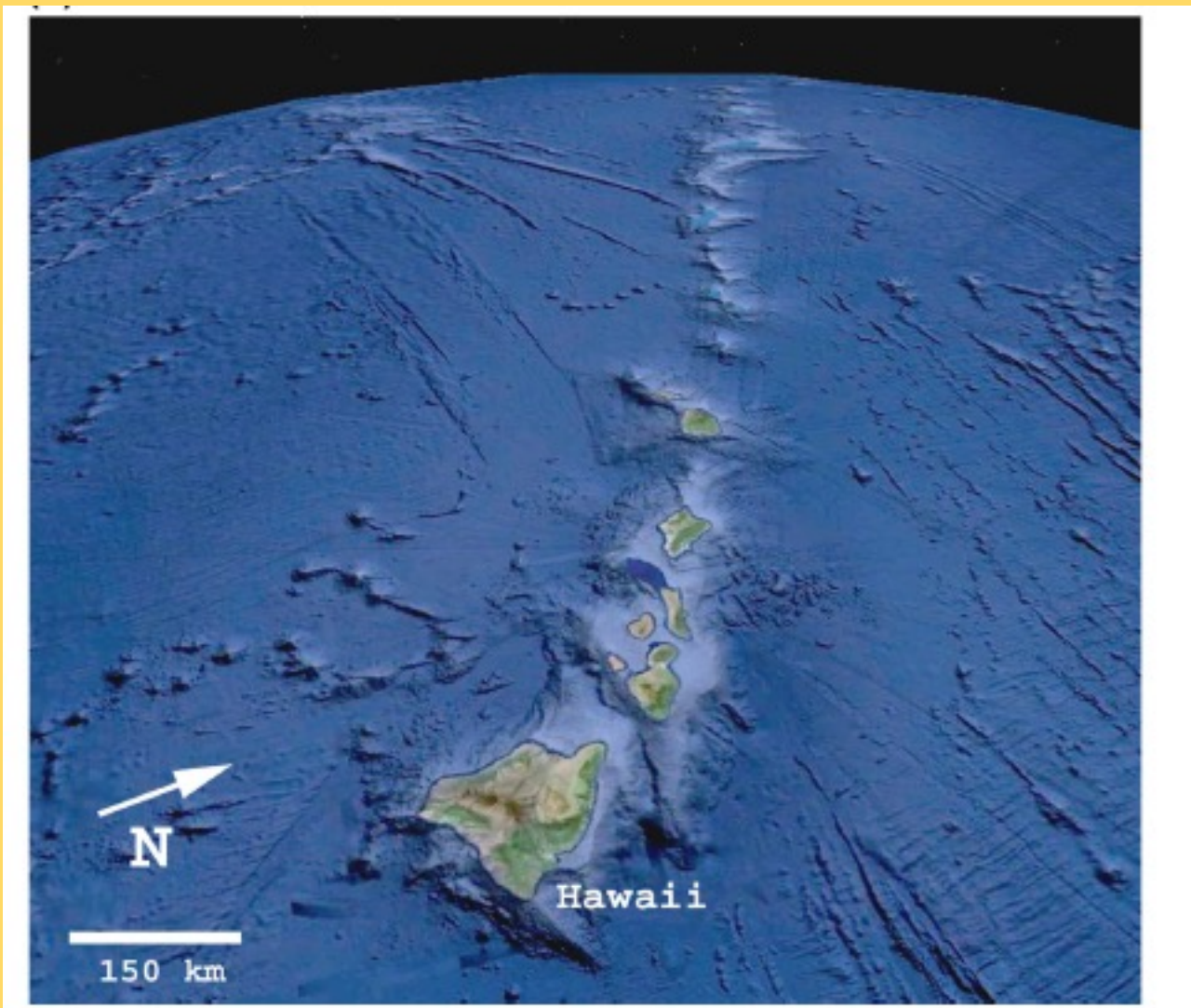


FIGURE 21.2 (a) Physiographic map of the Earth. This image was generated from digital databases of land and seafloor elevations on a 2 min latitude/longitude grid. Assumed illumination is from the west, and the projection is Mercator. Spatial resolution of the gridded data varies from true 2 min for the Atlantic, Pacific, and Indian Ocean floors and all land masses to 5 min for the Arctic Ocean floor. (Courtesy of NOAA.) (b) Volcanoes and the Crustal Plates Global map of the major tectonic plate boundaries and locations of the world's volcanoes. Courtesy of the US Geological Survey.

Pieri and Dziewonski, 2015

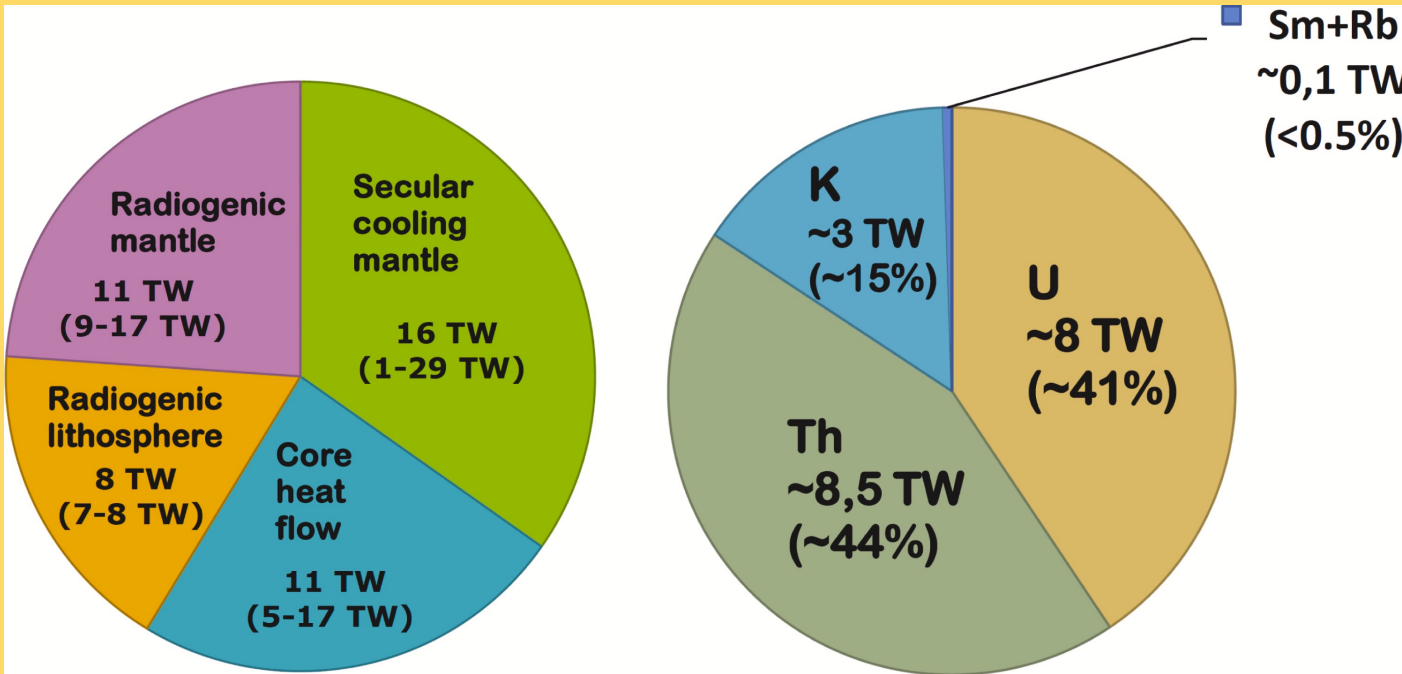
04&05/11/2022

Hawaii



Pieri and Dziewonski, 2015

Heat flux

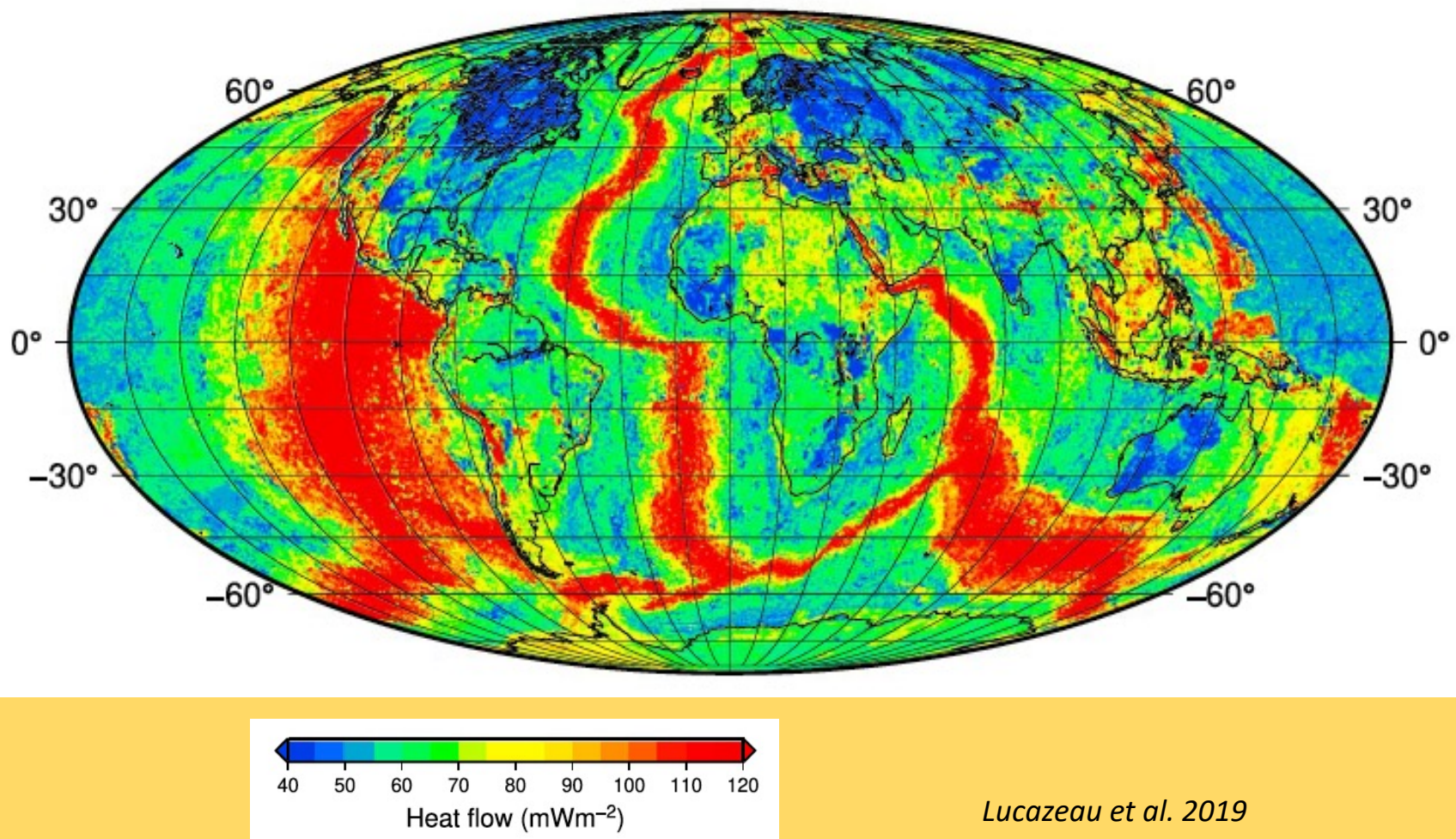


$$46 \pm 3 \text{ TW}$$

Jaupart and Mareschal, 2015

Measured heat flux

(b)

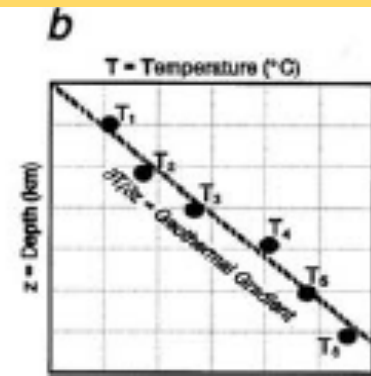
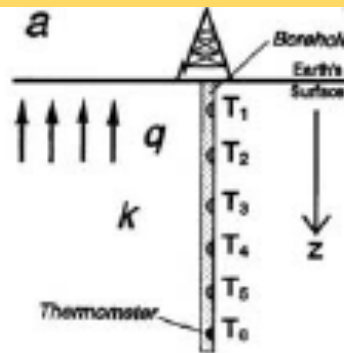


Lucazeau et al. 2019

Heat flux measurements

$$Q = -k \frac{\partial T}{\partial z}$$

k: thermal conductivity ($\text{W m}^{-2} \text{K}^{-1}$)



After Romanowicz, college de France

Heat transfer

Mechanisms of Heat Transfer - Convection

$q = h\Delta T$
where
 q is the local heat flux density [W.m^{-2}]
 h is the heat transfer coefficient [$\text{W.m}^{-2}.\text{K}$]
 ΔT is the temperature difference [K]

$q = -k\nabla T$
where
 q is the local heat flux density [W.m^{-2}]
 k is the materials conductivity [$\text{W.m}^{-1}.\text{K}^{-1}$]
 ∇T is the temperature gradient [K.m^{-1}]

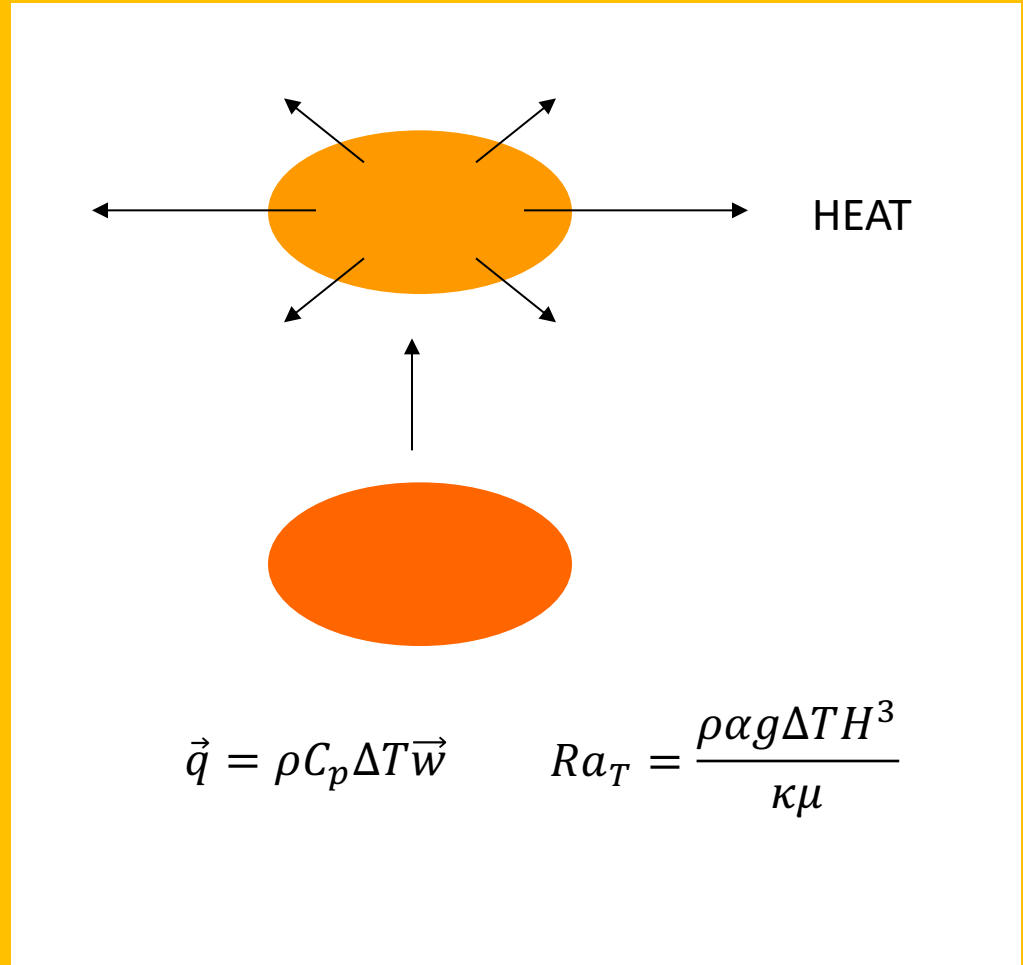
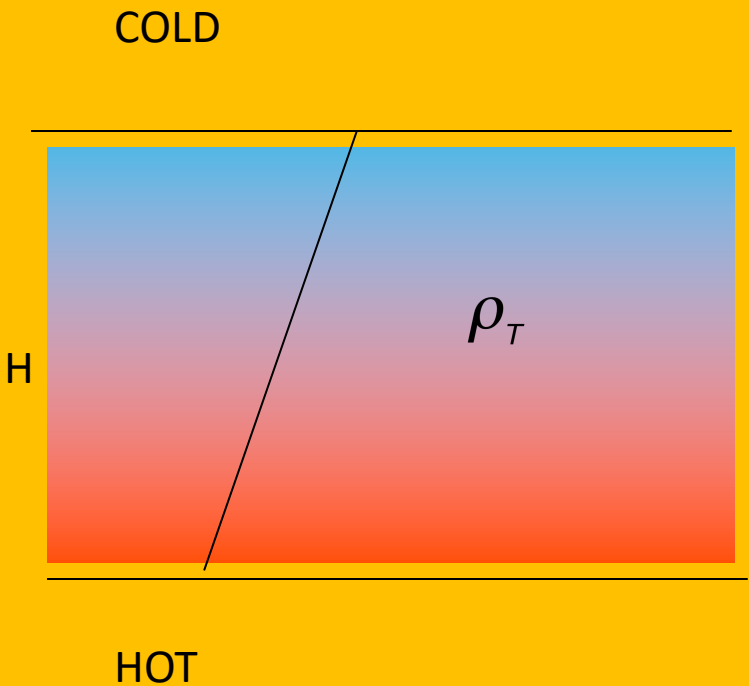
The diagram illustrates three mechanisms of heat transfer:

- Convection:** Shows a pot of water with bubbles rising from the bottom, indicating the movement of heated fluid.
- Conduction:** Shows a hand holding a metal rod, where heat is transferred through the material.
- Radiation:** Shows two hands with wavy arrows between them, representing the emission and absorption of infrared radiation.

$q = \varepsilon\sigma T^4$
where
 q is the power radiated from an object [W.m^{-2}]
 σ is the Stefan-Boltzmann constant [$\text{W.m}^{-2}\text{K}^4$]
 ε is the emissivity of the surface of a material [-]

<https://thermal-engineering.org/wp-content/uploads/2019/05/Convection-Conductive-Heat-Transfer-comparison-min.png>

Convection

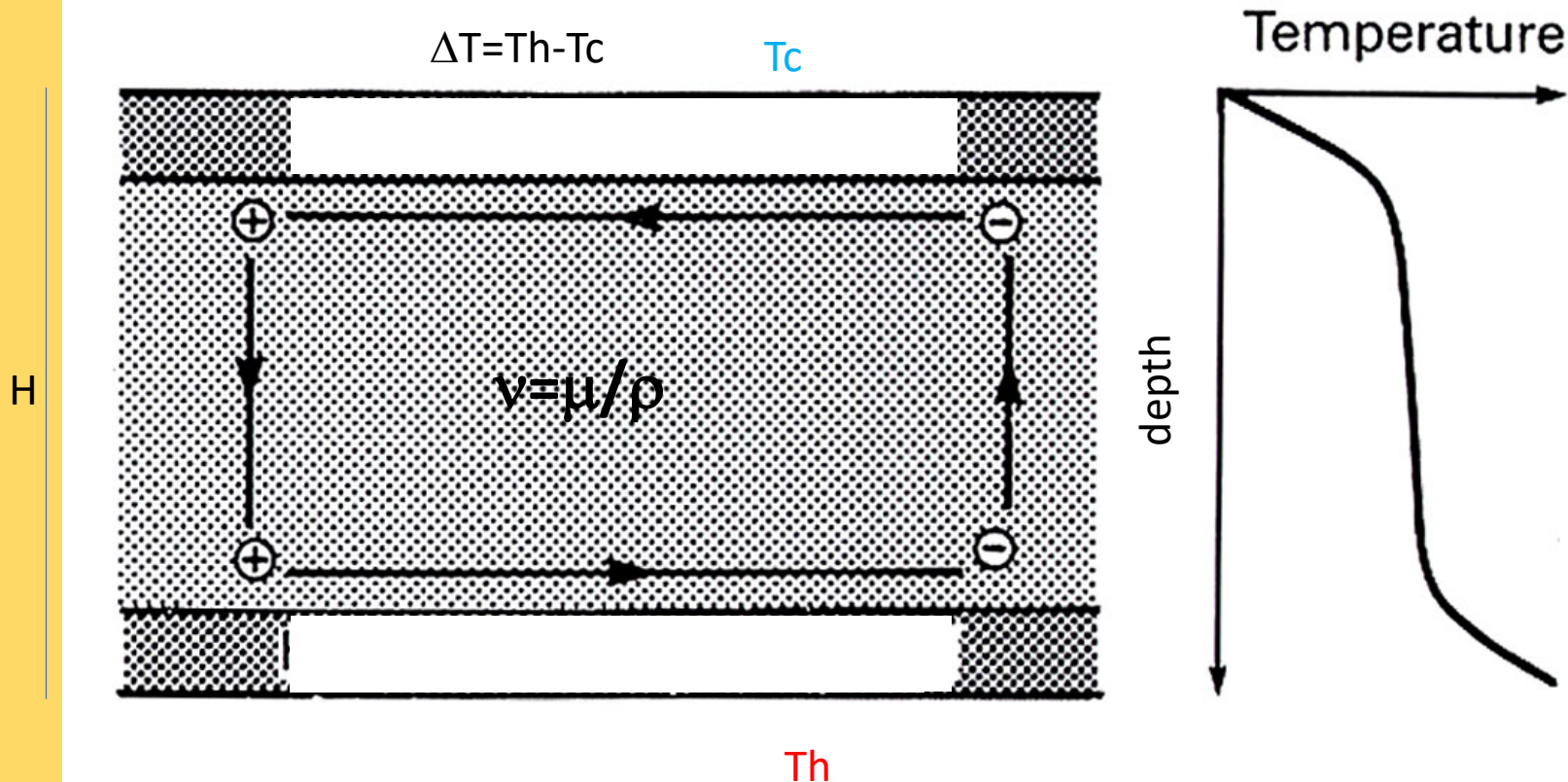


$$\vec{q} = \rho C_p \Delta T \vec{w} \quad Ra_T = \frac{\rho \alpha g \Delta T H^3}{\kappa \mu}$$

Thermal Convection

$$Ra(H, \Delta T) = \frac{\alpha g \Delta T H^3}{\kappa \nu}$$

With c , the thermal expansion coefficient and κ thermal diffusivity



D'après Barbara Romanowicz, collège de France 2014: <http://www.college-de-france.fr/site/barbara-romanowicz/course-2013-2014.htm>

Thermal Convection patterns for different Rayleigh numbers

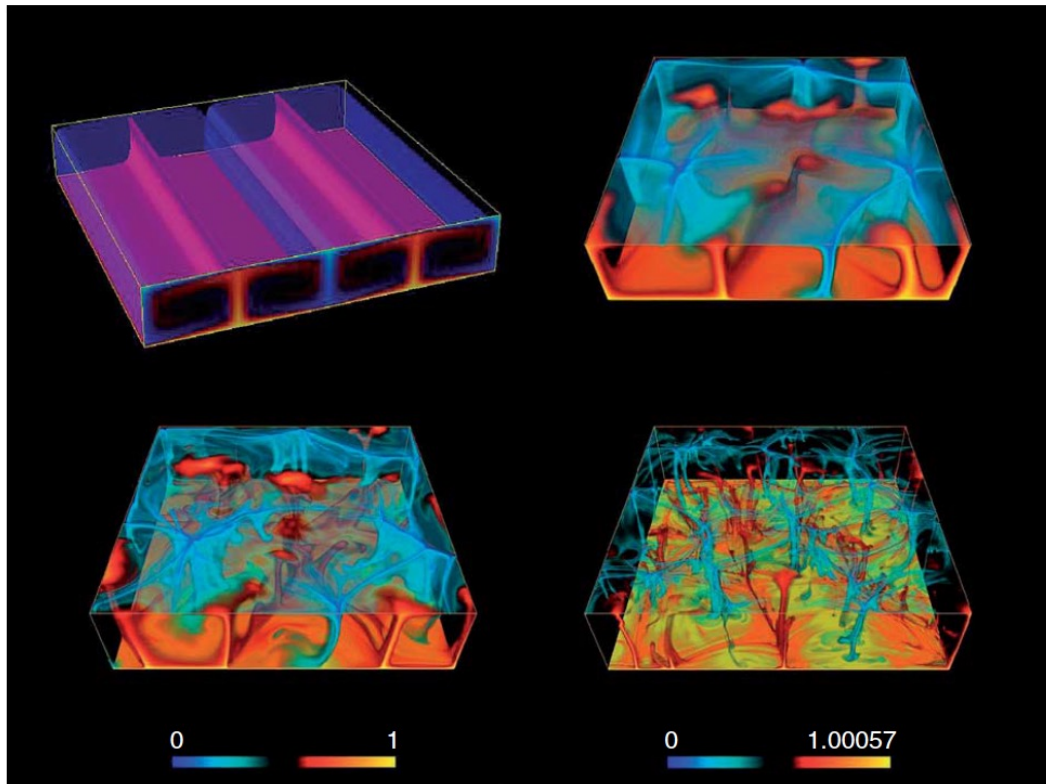


Figure 4 Convection patterns of a fluid heated from below at Rayleigh number 10^5 , 10^6 , 10^7 , 10^8 . The temperature color bars range from 0 (top boundary) to 1 (bottom boundary). The Boussinesq approximation was used (numerical simulations by F. Dubuffet). The increase in Rayleigh number corresponds to a decrease of the boundary layer thicknesses and the width of plumes. Only in the case of the lowest Rayleigh number (top left) is the convection stationary with cells of aspect ratio $\sim \sqrt{2}$ as predicted by marginal stability. For higher Rayleigh number, the patterns are highly time dependent.

$$Ra(H, \Delta T) = \frac{\alpha g \Delta T H^3}{\kappa \nu}$$

Question:

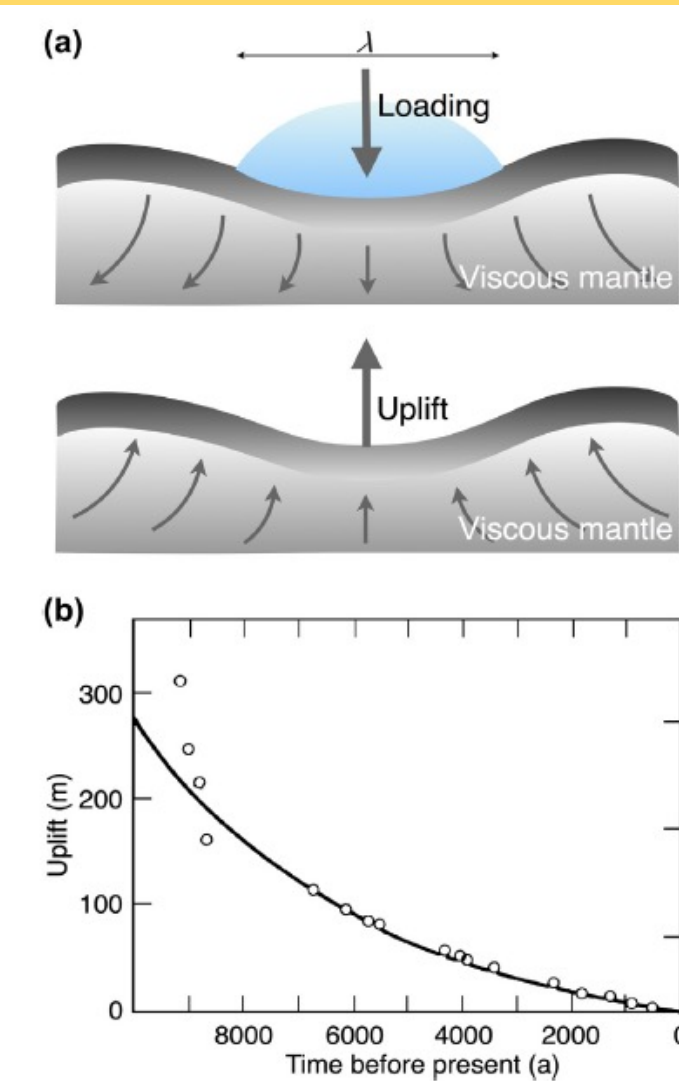
What is the Rayleigh number of the Earth mantle?

Ricard, 2007

Viscosity of the mantle

Viscosity depends on:

- Process of deformation (diffusion, dislocation)
- T, grain size, water content



$$\tau = \frac{4\pi\eta}{\rho g \lambda},$$

Breuer et spohn, 2015

FIGURE 9.5 (a) Surface subsidence due to loading of an ice sheet of characteristic wavelength λ and subsequent viscous uplift following rapid ice melting. (b) Data points for the uplift h of the mouth of the Angerman River, Sweden, as a function of time before present compared with an exponential relaxation model of the kind $h \sim \exp(-t/\tau)$, with τ defined as in Eqn (9.3). After Turcotte and Schubert (2002).

Viscosity in the Earth

Material	Viscosity (Pa s)
Water (20 °C)	10^{-3}
Basalt (1100 °C)	400
Ice (0 °C)	10^{11}
Ice (-20 °C)	10^{13}
Granite	10^{23}
Lithosphere	10^{23} - 10^{24}
Asthenosphere	10^{19} - 10^{20}
Outer core	10^{-2}

Thermal profile in the Earth

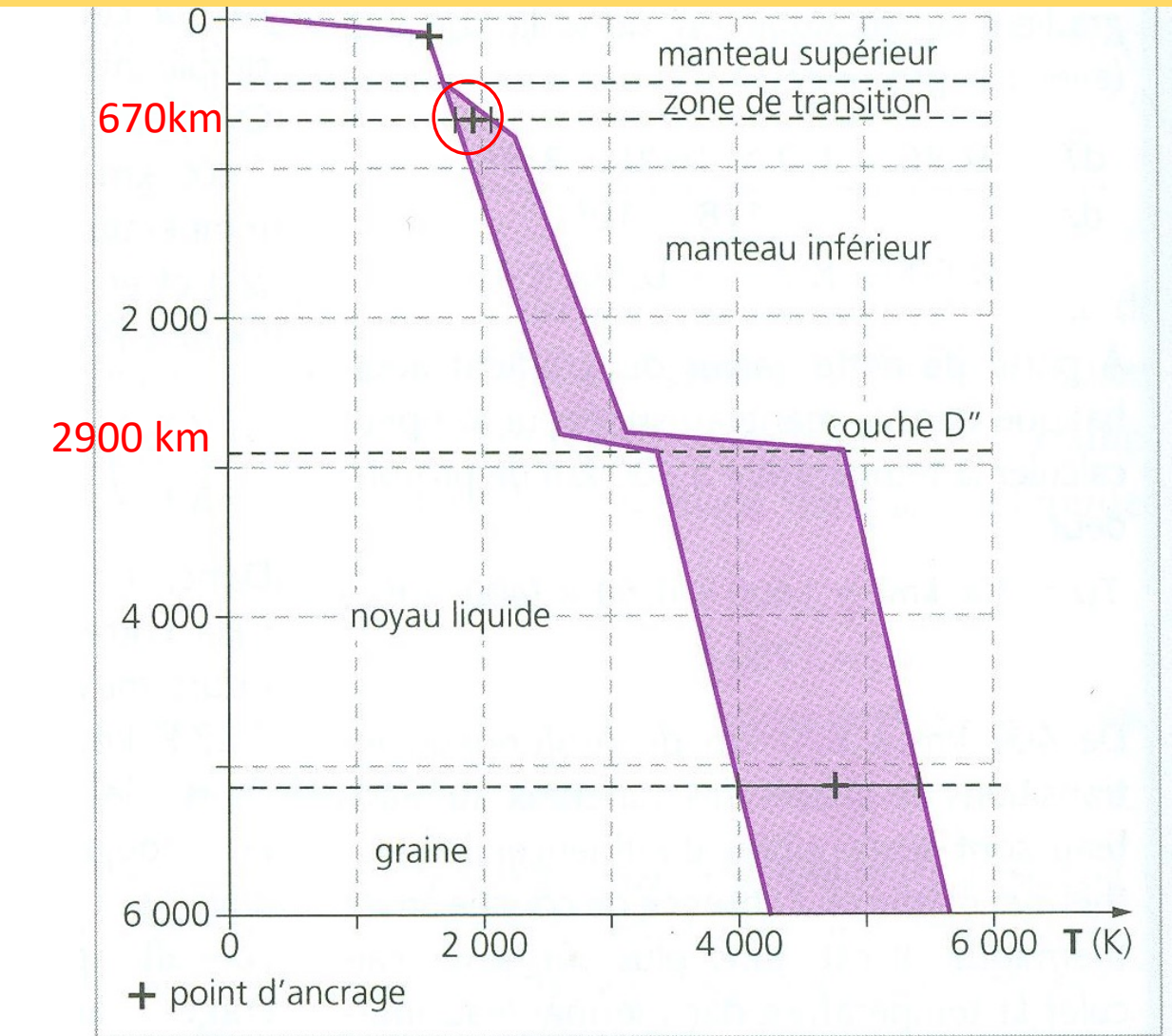


Fig. 2.14. Géotherme calculé à partir de trois points d'ancrage et du gradient adiabatique.

i/11/2022

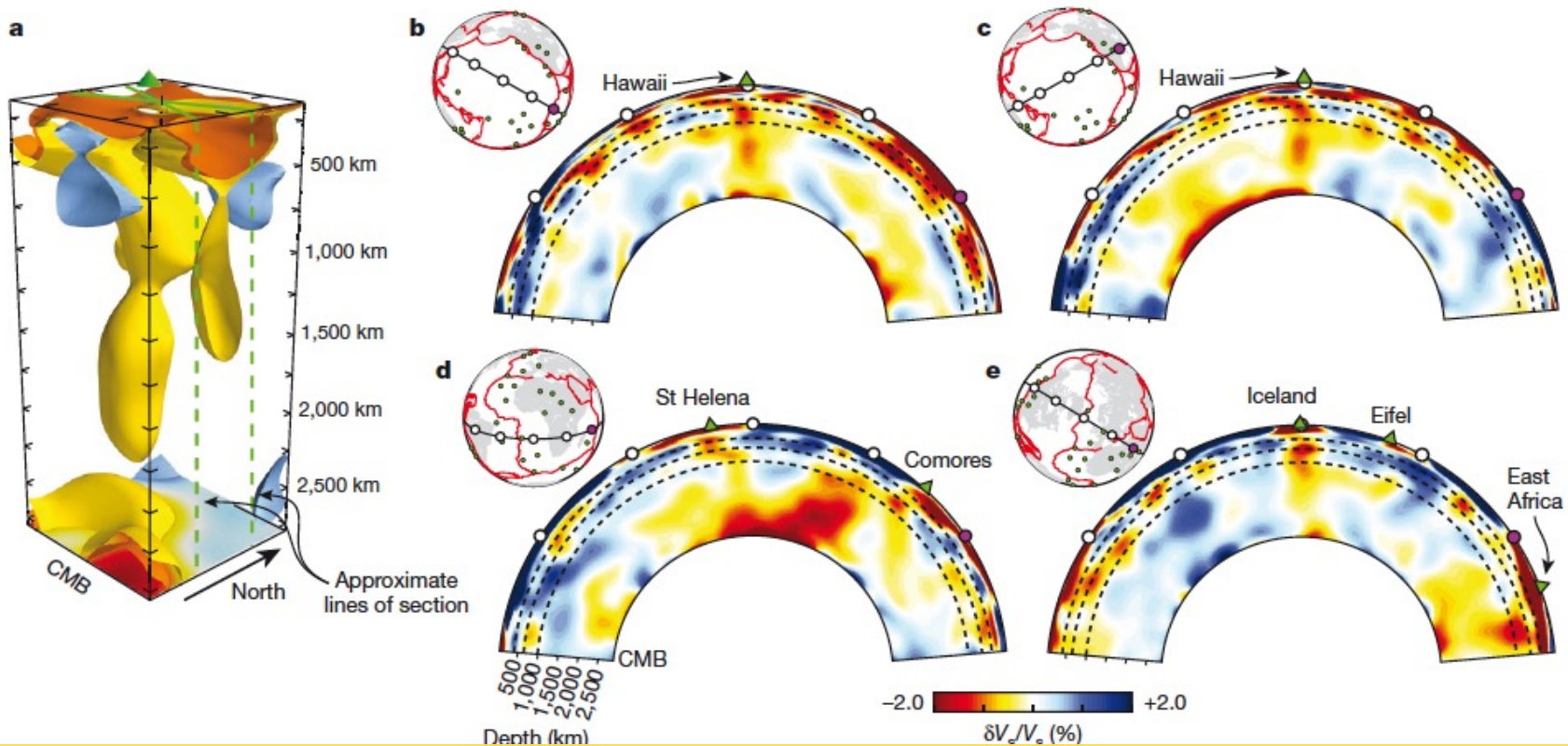
Les houches – Solid Earth

$$2000 < \Delta T < 5000$$

$$10^6 < Ra < 10^8$$

From: Dewaele et Sanloup, éds
Belin: l'Intérieur de la Terre et des planètes

Seismological evidences

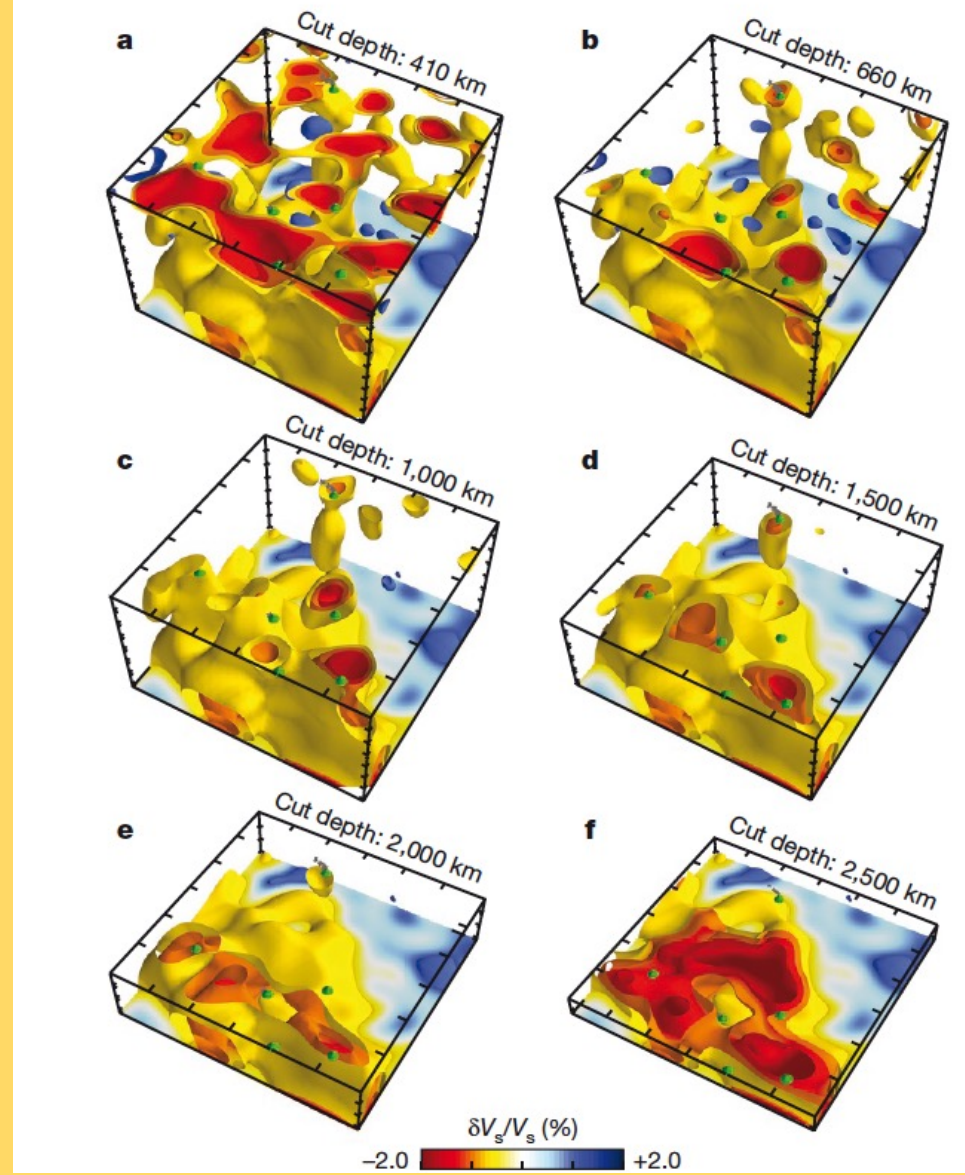


French and Romanowicz, 2015

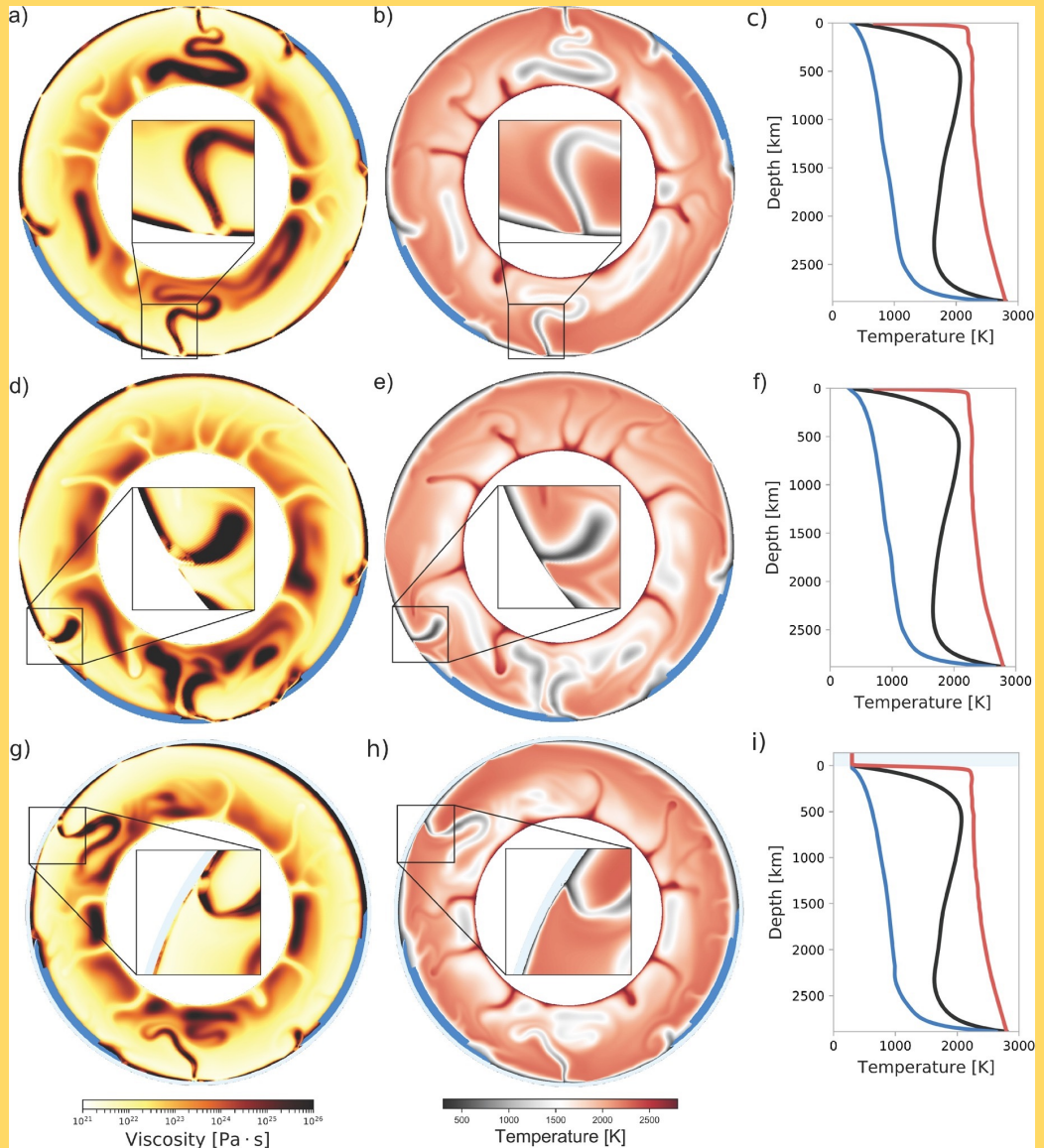
Seismological evidences

large low shear velocity provinces
(LLSVPs),

French and Romanowicz, 2015

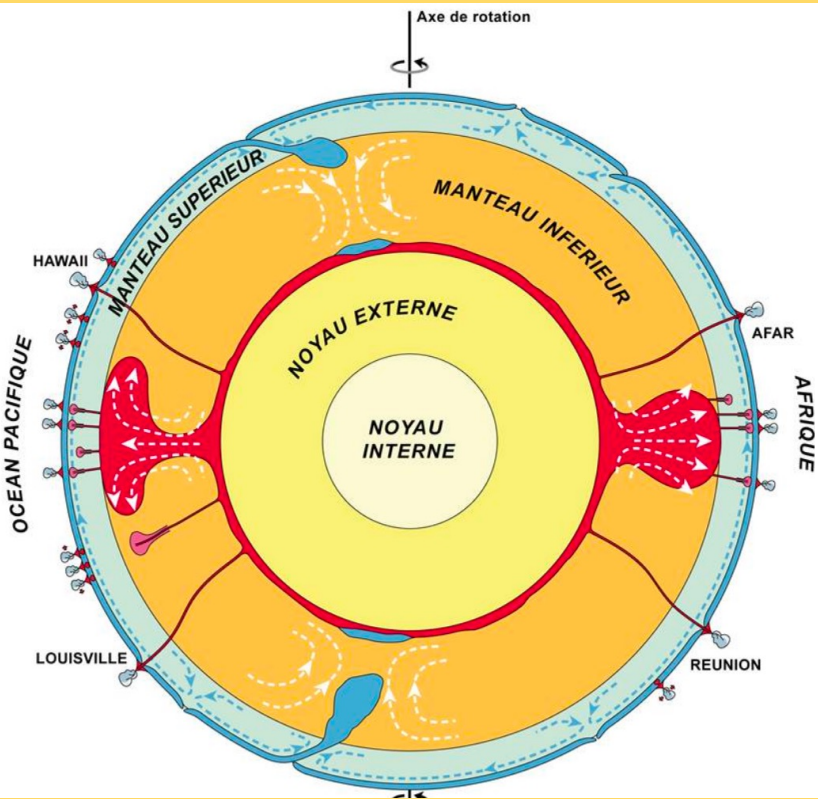


Numerical models



Where does subduction initiate and cease? A global scale perspective
[Ulyrova et al., 2019, EPSL.](#)

Schematic view of geodynamics on Earth



Courtillot et al., 2003

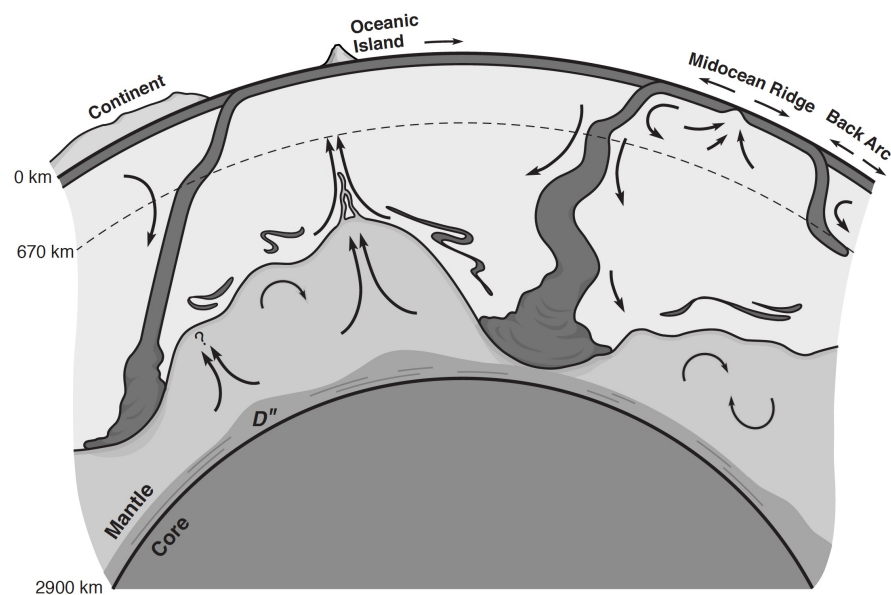


Fig. 1. Diagram illustrating the possible dynamics of an intrinsically dense layer in the lower mantle. Depth to the top of the layer ranges from ~1600 km to near the CMB, where it is deflected by downwelling slabs. Internal circulation within the layer is driven by internal heating and by heat flow across the CMB. A thermal boundary layer develops at the interface, and plumes arise from local high spots, carrying recycled slab and some primordial material.

Kellogg et al., 1999

Schematic view of geodynamics on Earth

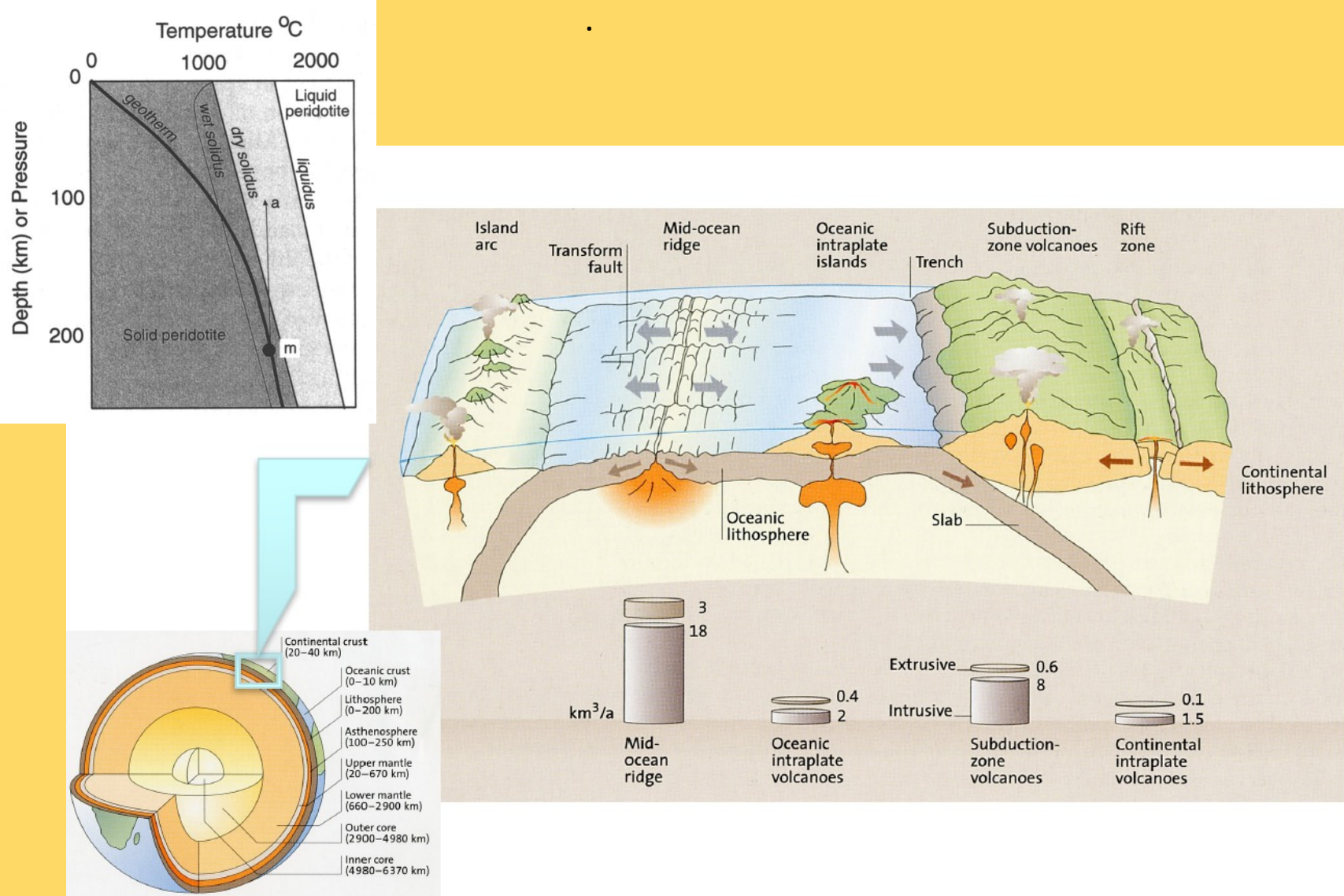
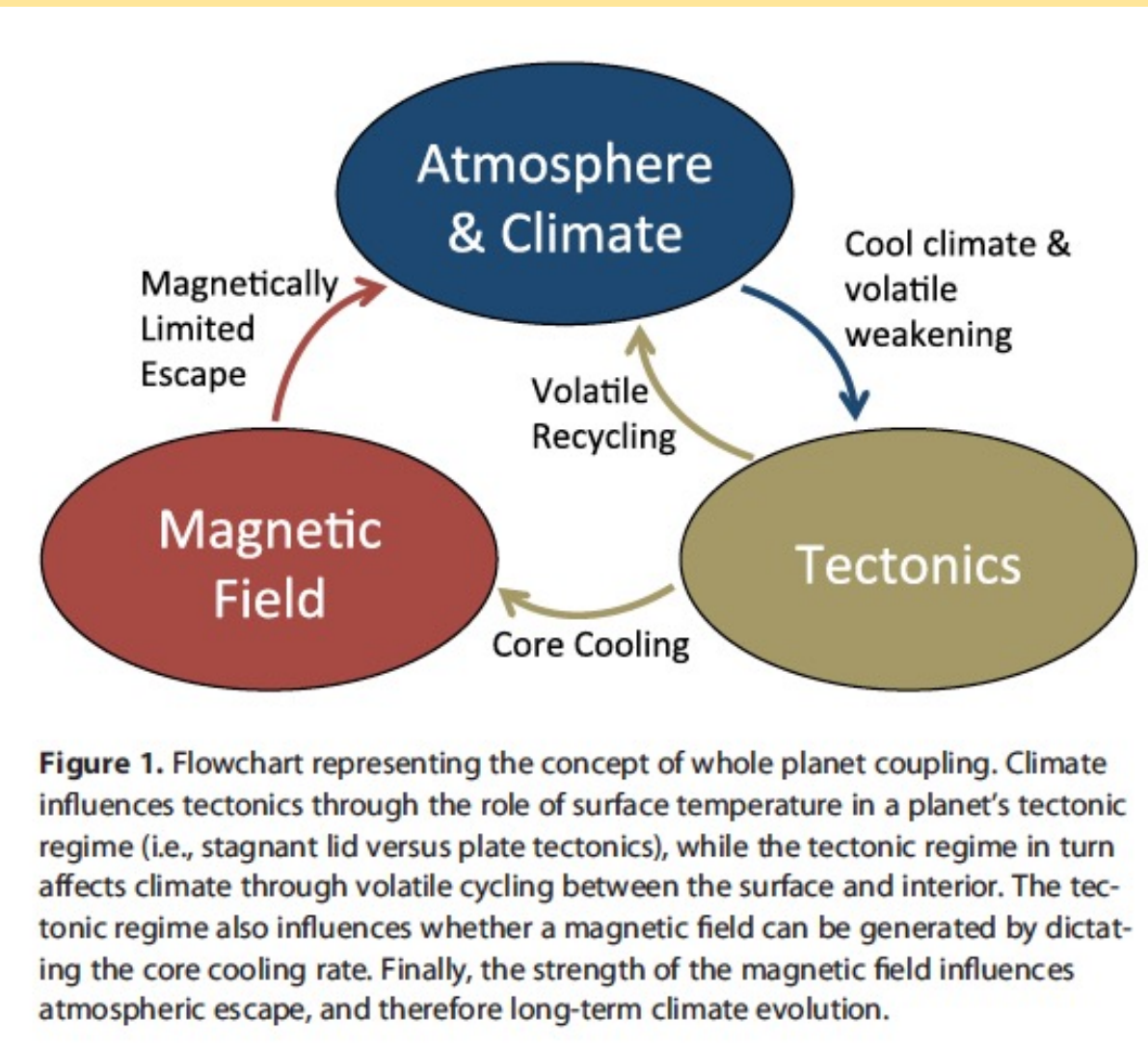


Plate tectonics and habitability



Foley and Driscoll, 2016

Plate tectonics and habitability

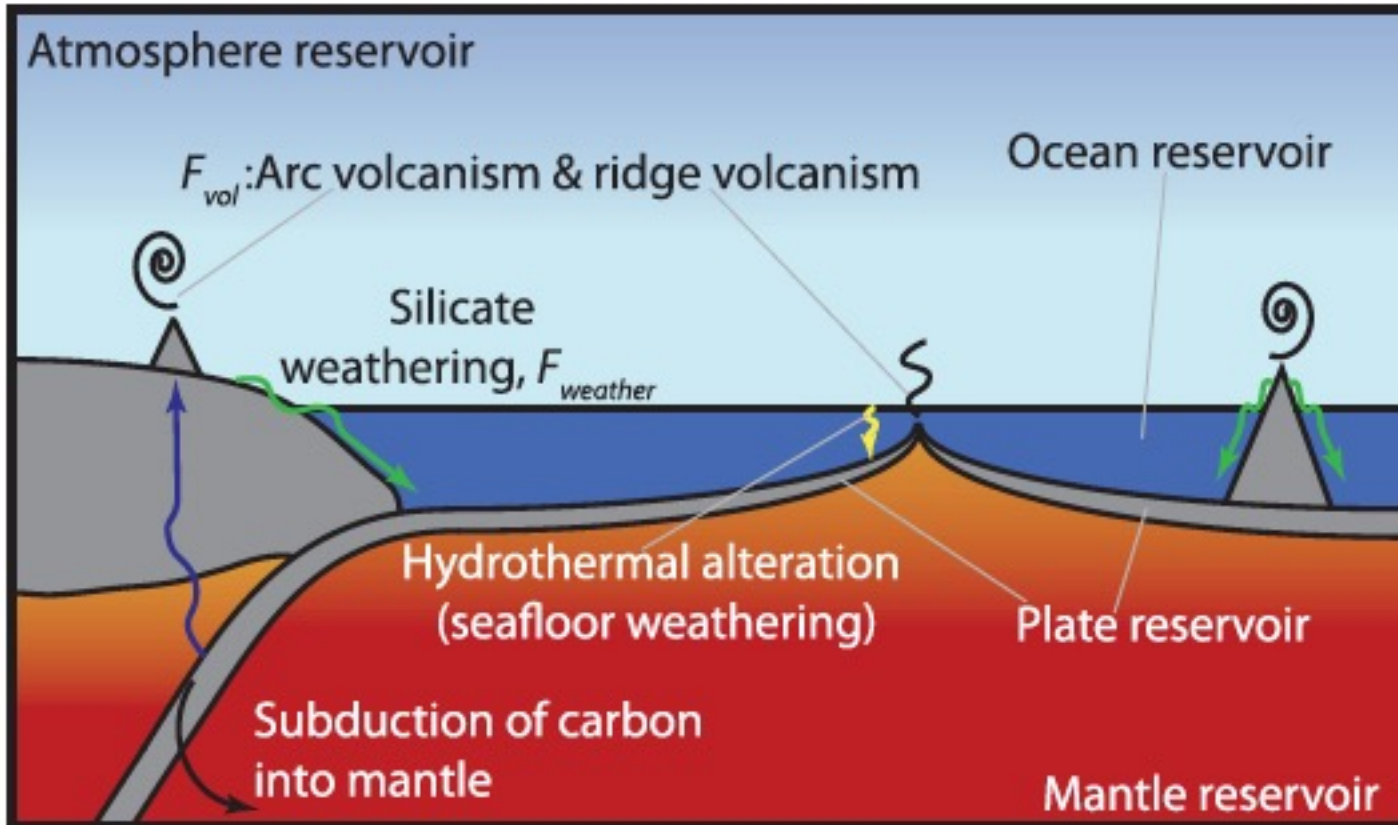


Figure 4. Schematic diagram of the global carbon cycle after Foley [2015].

Foley and Driscoll, 2016

Plate tectonics and habitability

Other planets?

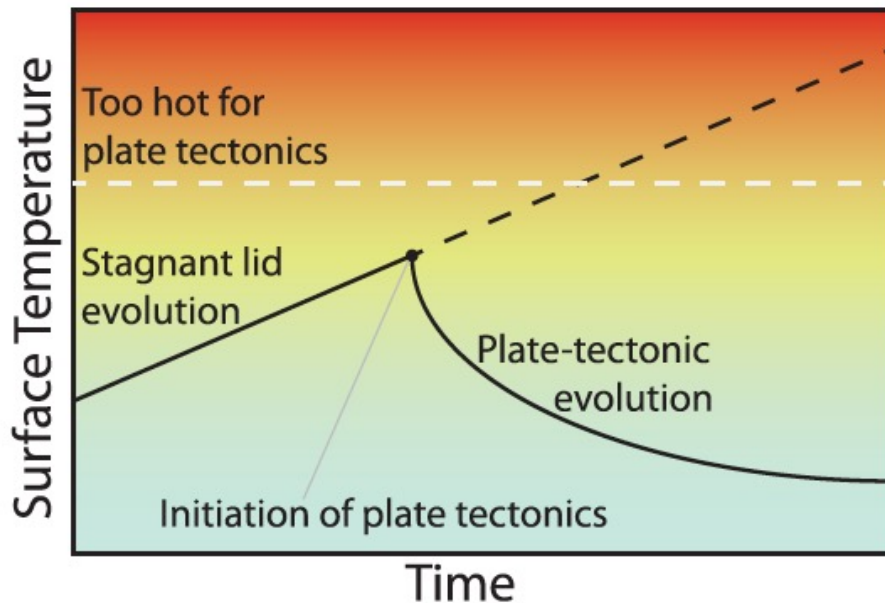


Figure 12. Schematic diagram of the divergence point in planetary evolution involving the initiation of plate tectonics. Before plate tectonics, a planet's weathering rate may be supply limited, such that surface temperature climbs over time as a result of increasing luminosity. Once plate tectonics initiates, silicate weathering is enhanced by higher erosion rates and continent formation, and climate cools.